

**A high resolution model of linear trend in mass variations from DMT-2  
Added value of accounting for coloured noise in GRACE data**

Farahani, Hassan Hashemi; Ditmar, Pavel; Inácio, Pedro; Didova, Olga; Gunter, Brian; Klees, Roland; Guo, X.; Guo, Jing; Sun, Yu; Liu, Xianglin

**DOI**

[10.1016/j.jog.2016.10.005](https://doi.org/10.1016/j.jog.2016.10.005)

**Publication date**

2017

**Document Version**

Accepted author manuscript

**Published in**

Journal of Geodynamics

**Citation (APA)**

Farahani, H. H., Ditmar, P., Inácio, P., Didova, O., Gunter, B., Klees, R., Guo, X., Guo, J., Sun, Y., Liu, X., Zhao, Q., & Riva, R. (2017). A high resolution model of linear trend in mass variations from DMT-2: Added value of accounting for coloured noise in GRACE data. *Journal of Geodynamics*, 103, 12-25.  
<https://doi.org/10.1016/j.jog.2016.10.005>

**Important note**

To cite this publication, please use the final published version (if applicable).  
Please check the document version above.

**Copyright**

Other than for strictly personal use, it is not permitted to download, forward or distribute the text or part of it, without the consent of the author(s) and/or copyright holder(s), unless the work is under an open content license such as Creative Commons.

**Takedown policy**

Please contact us and provide details if you believe this document breaches copyrights.  
We will remove access to the work immediately and investigate your claim.

## A high resolution model of linear trend in mass variations from DMT-2: added value of accounting for coloured noise in GRACE data

Hassan H. Farahani<sup>a,\*</sup>, Pavel Ditmar<sup>a</sup>, Pedro Inácio<sup>a</sup>, Olga Didova<sup>a</sup>, Brian Gunter<sup>a,b</sup>, Roland Klees<sup>a</sup>, Xiang Guo<sup>a,c</sup>, Jing Guo<sup>c</sup>, Yu Sun<sup>a</sup>, Xianglin Liu<sup>a,d</sup>, Qile Zhao<sup>c</sup>, Riccardo Riva<sup>a</sup>

<sup>a</sup>*Delft University of Technology, Stevinweg 1, 2628 CN, Delft, The Netherlands*

<sup>b</sup>*Georgia Institute of Technology, 270 Ferst Dr. NW, Atlanta, GA 30332-0150, USA*

<sup>c</sup>*GNSS Research Center, Wuhan University, 129 Luoyu Rd., Wuhan 430079, China*

<sup>d</sup>*Fugro Intersite B.V., Dillenburgsingel 69, 2263 HW, Leidschendam, The Netherlands*

---

### Abstract

We present a high resolution model of the linear trend in the Earth's mass variations based on DMT-2 (Delft Mass Transport model, release 2). DMT-2 was produced primarily from K-Band Ranging (KBR) data of the Gravity Recovery And Climate Experiment (GRACE). It comprises a time series of monthly solutions complete to spherical harmonic degree 120. A novel feature in its production was the accurate computation and incorporation of stochastic properties of coloured noise when processing KBR data. The unconstrained DMT-2 monthly solutions are used to estimate the linear trend together with a bias, as well as annual and semi-annual sinusoidal terms. The linear term is further processed with an anisotropic Wiener filter, which uses full noise and signal covariance matrices. Given the fact that noise in an unconstrained model of the trend is reduced substantially as compared

---

\*Corresponding author

*Email address:* [h.hashemi@tudelft.nl](mailto:h.hashemi@tudelft.nl) (Hassan H. Farahani)

to monthly solutions, the Wiener filter associated with the trend is much less aggressive compared to a Wiener filter applied to monthly solutions. Consequently, the trend estimate shows an enhanced spatial resolution. It allows signals in relatively small water bodies, such as Aral sea and Ladoga lake, to be detected. Over the ice sheets, it allows for a clear identification of signals associated with some outlet glaciers or their groups. We compare the obtained trend estimate with the ones from the CSR-RL05 model using (i) the same approach based on monthly noise covariance matrices and (ii) a commonly-used approach based on the DDK-filtered monthly solutions. We use satellite altimetry data as independent control data. The comparison demonstrates a high spatial resolution of the DMT-2 linear trend. We link this to the usage of high-accuracy monthly noise covariance matrices, which is due to an accurate computation and incorporation of coloured noise when processing KBR data. A preliminary comparison of the linear trend based on DMT-2 with that computed from GSFC\_global\_mascons\_v01 reveals, among other, a high concentration of the signal along the coast for both models in areas like the ice sheets, Gulf of Alaska, and Iceland.

*Keywords:* Time varying gravity field, GRACE, KBR, DMT-2, Coloured noise

---

## 1. Introduction

Temporal variations of the Earth's gravity field at various spatial scales are known to be caused by mass re-distribution due to megathrust earthquakes (e.g., Han et al., 2006, 2011), accumulation and depletion of continental water stocks (e.g., Wahr et al., 1998; Swenson et al., 2003; Klees et

6 al., 2007, 2008a), postglacial rebound (e.g., van der Wal et al., 2008; Gunter  
7 et al., 2014), ice mass losses in the polar areas (e.g., Luthcke et al., 2006;  
8 Wouters et al., 2008; Baur and Sneeuw, 2011; Rignot and Mouginot, 2012;  
9 Siemes et al., 2013), and the subsequent sea level rise (e.g., Bamber et al.,  
10 2009). The primary tool to observe the large-scale mass variations is currently  
11 the Gravity Recovery And Climate Experiment (GRACE) satellite mission,  
12 which has been operational since March 2002 (Tapley et al., 2004a,b). The  
13 K-Band Ranging (KBR) data, collected by this mission, in conjunction with  
14 its other measurements, i.e., GPS (Global Positioning System), attitude, and  
15 accelerometer data, are processed by different research centres, and various  
16 models of time-variations are computed (e.g., Bettadpur, 2007, 2012; Flecht-  
17 ner, 2007; Watkins and Yuan, 2007, 2012; Kurtenbach et al., 2009; Dahle et  
18 al., 2012; Bruinsma et al., 2010; Liu, 2008; Liu et al., 2010; Mayer-Gürr et al.,  
19 2010a,b, 2014; Meyer et al., 2012; Chen et al., 2015). The majority of models  
20 make use of spherical harmonics (e.g., Heiskanen and Moritz, 1967) and are  
21 complete to degree 60 – 120, which corresponds to spatial scales larger than  
22 165 – 330 km (half-wavelength). Some other models, e.g., those produced  
23 by Luthcke et al. (2013) and Watkins et al. (2015), are based on mass con-  
24 centration blocks, i.e., so-called mascons parametrization. They are vastly  
25 believed to improve the spatial resolution further as compared to spherical  
26 harmonic models of the mass transport (Watkins et al., 2015). The temporal  
27 sampling of GRACE-based models is typically one month.

28       Recently, Delft University of Technology, in collaboration with the GNSS  
29 Research Centre of Wuhan University, has compiled and released a new spher-  
30 ical harmonic model entitled DMT-2: Delft Mass Transport model, release

31 2 (Farahani, 2013). Similar to its predecessor DMT-1 (Liu, 2008; Liu et al.,  
32 2010), the new model consists of a time series of monthly solutions complete  
33 to degree 120. Both unconstrained and constrained (i.e., filtered) solutions  
34 are available. In the latter case, an anisotropic Wiener-type filter devel-  
35 oped by Klees et al. (2008b) is applied to suppress noise, which is primarily  
36 caused by an anisotropic sensitivity of the KBR data and manifests itself in  
37 the form of pronounced along-track artifacts, i.e., the well-known “stripes”.  
38 The filter is based on the full signal and noise covariance matrices. It is  
39 designed as a mean square error filter of monthly mass re-distribution. It  
40 is a spatially-varying filter, meaning that the smoothing is minimal in areas  
41 where signal is strong (i.e., the lower the noise, the less smoothing, and vice  
42 versa). Unlike in DMT-1, degree-1 coefficients are restored in the DMT-2  
43 monthly solutions using a modified version of the approach of Swenson et  
44 al. (2008), which is described in (Sun et al., 2016). A novel feature of the  
45 methodology designed to produce DMT-2 is an accurate computation and  
46 incorporation of stochastic properties of coloured noise when processing KBR  
47 data. This leads to an accurate computation of noise covariance matrices,  
48 which enter Wiener filters. With this manuscript, we use DMT-2 to compute  
49 new models of the long-term linear trend in mass variations, which vary in  
50 terms of maximum spherical harmonic degree. To that end, we follow the  
51 methodology developed by Siemes et al. (2013). It is, in essence, a further  
52 development of the filtering idea of Klees et al. (2008b). It is realized by a  
53 design and application of an anisotropic Wiener-type filter to the linear trend  
54 obtained from unconstrained monthly solutions. That is, it is designed as a  
55 mean square error filter of linear trends in mass re-distribution. For com-

56 parison, we additionally produce a filtered linear trend from the CSR-RL05  
57 monthly solutions (Bettadpur, 2012) and their noise covariance matrices,  
58 using the same methodology. In addition, we compute the linear trend in  
59 line with a commonly-used approach, i.e., using monthly solutions subject  
60 to DDK de-correlating non-isotropic filtering (Kusche, 2007; Kusche et al.,  
61 2009). We assess the models of the linear trend with satellite altimetry data.  
62 The comparison allows us to study the added value of the applied Wiener  
63 filter. It additionally allows for an analysis of the added value of accounting  
64 for coloured noise when processing KBR data, which is currently done in  
65 the production of only a few spherical harmonic time-varying gravity field  
66 models, namely, DMT-2 and those produced in line with Mayer-Gürr (2006)  
67 and Mayer-Gürr et al. (2010a). Finally, we make a preliminary comparison  
68 of the linear trend model based on DMT-2 with one produced with a latest  
69 mascon implementation, namely, GSFC\_global\_mascons\_v01 (Luthcke et al.,  
70 2013).

71 The manuscript is outlined as follows. Section 2 (in conjunction with  
72 Appendix A) describes the computation of DMT-2 monthly unconstrained  
73 solutions. In Section 3, we compute and assess the model of the linear trend.  
74 A brief description of how it is computed from the monthly solutions is also  
75 presented there. Finally, in Section 4, we conclude by emphasizing the main  
76 findings and identifying topics for future research.

## 77 **2. DMT-2**

78 DMT-2 consists of monthly gravity field solutions spanning the time in-  
79 terval February 2003 – December 2011. Three months (June 2003, January

80 2011, and June 2011) are excluded due to a complete or a partial lack of  
81 GRACE data. The solutions consist of residual spherical harmonic coeffi-  
82 cients with respect to the static gravity field model DGM-1S: Delft Gravity  
83 Model, release 1, satellite-only (Farahani et al., 2013a,b). The coefficients  
84 were estimated by a stand-alone inversion of KBR data. The unconstrained  
85 procedure consisted of two steps: (1) transforming KBR data into residual  
86 gravity data (cf. Appendix A) with respect to the a priori model; and (2)  
87 inverting these residuals into residual spherical harmonic coefficients using  
88 the least-squares adjustment in a statistically optimal manner. The first step  
89 was done mostly in the same way as in the case of DMT-1. For the complete-  
90 ness, we briefly describe it in Appendix A. A novel element of the second  
91 step was an accurate computation and parameterization of coloured noise in  
92 KBR data, which is described below.

93 Residual range combinations are contaminated by frequency-dependent  
94 (i.e., coloured) noise (e.g., Liu et al., 2010). To account for this, frequency-  
95 dependent data weighting (e.g., Klees et al., 2003; Klees and Ditmar, 2004)  
96 was used. This ensures a statistically optimal inversion of the residual data,  
97 provided that (i) an accurate realization of their noise is obtained and (ii) the  
98 stochastic properties of the noise are modeled properly. To realize the lat-  
99 ter, Auto-Regressive Moving-Average (ARMA) noise models, whose Power  
100 Spectral Densities (PSDs) best fit PSDs of the noise, were built (Klees and  
101 Broersen, 2002; Klees et al., 2003). Noise realizations were produced iter-  
102 atively as described in the following. The residual data themselves were  
103 assumed to be initial noise realizations. This allowed initial ARMA models  
104 to be produced, which resulted in preliminary monthly gravity field solu-

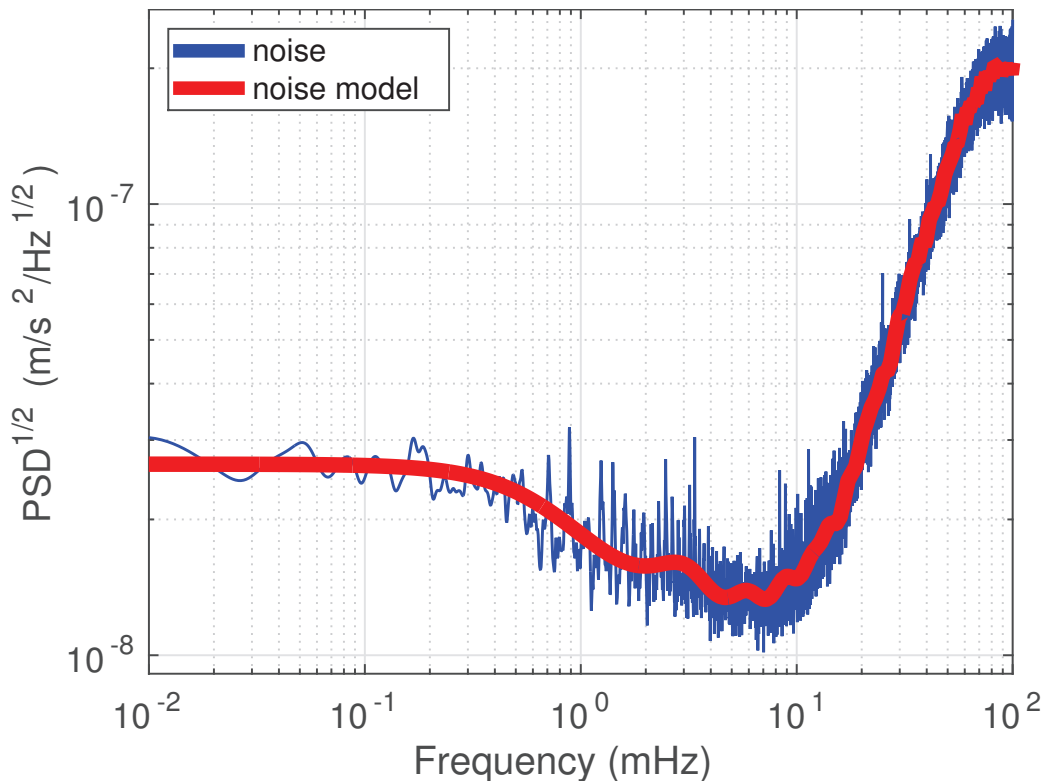


Figure 1: The PSD<sup>1/2</sup> of noise and of stochastic model of noise in residual range combinations for July 2006.

105 tions. The corresponding sets of a posteriori residuals were used as improved  
 106 realizations of noise. No additional iterations of this kind were necessary, as  
 107 further changes in the estimated noise properties were found to be negligible.  
 108 As an example, Fig. 1 shows the PSD<sup>1/2</sup> of noise in residual range combina-  
 109 tions in July 2006 together with its best-fitting ARMA model, which is in  
 110 this instance an Auto-Regressive (AR) one of order 79. Such a model of  
 111 noise was built for each month individually. In this way, gradual changes  
 112 in the noise characteristics were captured. We found that those changes are  
 113 particularly pronounced in the frequency range 0.5 – 10 mHz (3 – 54 cycles



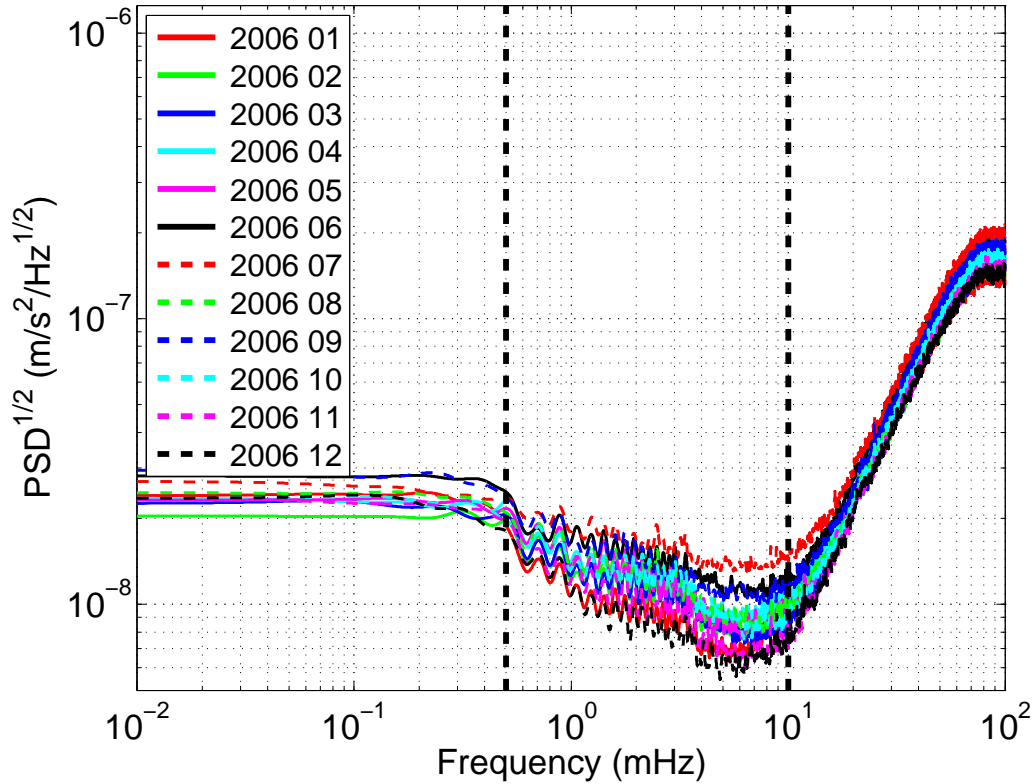


Figure 2: The noise  $\text{PSD}^{\frac{1}{2}}$ s in the residual range combinations in 2006. The vertical lines mark the frequencies 3 and 54 cpr.

114 per revolution, cpr). This frequency range corresponds to signals at spatial  
 115 scales of 400 – 7200 km (half-wavelength), which comprise a significant part  
 116 of the time-varying gravity field. In Fig. 2, for instance, noise  $\text{PSD}^{\frac{1}{2}}$ s of  
 117 residual range combinations are shown for different months in 2006. Further  
 118 details about the adopted procedure can be found in (Farahani et al., 2014).

119

120 **3. Linear trend**

121 We begin with a brief description of the methodology followed to compute  
122 different variants of the linear trend (Section 3.1). The comparison of the  
123 results are provided in Section 3.2.

124 *3.1. Methodology*

125 We compute the constrained linear trend in line with the methodology  
126 developed by Siemes et al. (2013). To that end, we first compute an uncon-  
127 strained model of the linear trend, together with a bias, as well as annual and  
128 semi-annual (co-) sinusoidal terms, from the unconstrained DMT-2 monthly  
129 solutions. Furthermore, we propagate noise covariance matrices of the un-  
130 constrained monthly solutions onto the linear trend noise covariance matrix.  
131 In doing so, so-called formal noise covariance matrices are used, i.e., those ob-  
132 tained from the estimation process without any correction or scaling. Finally,  
133 we compute the constrained model of the linear trend with the Wiener-type  
134 filter of Klees et al. (2008a)

$$\mathbf{F} = \{(\mathbf{C}_{\hat{\mathbf{x}}})^{-1} + \mathbf{D}^{-1}\}^{-1}(\mathbf{C}_{\hat{\mathbf{x}}})^{-1}, \quad (1)$$

135 or equivalently

$$\mathbf{F} = \mathbf{D}\{\mathbf{C}_{\hat{\mathbf{x}}} + \mathbf{D}\}^{-1}, \quad (2)$$

136 based on the full signal covariance matrix  $\mathbf{D}$  and the full noise covariance  
137 matrix  $\mathbf{C}_{\hat{\mathbf{x}}}$  of the linear trend. To compute  $\mathbf{D}$  as reliably as possible, the time  
138 span for which the linear trend is to be estimated is divided into multiple  
139 intervals of the same length. This allows us to obtain multiple intermediate  
140 samples of the linear trend, from which an estimate of  $\mathbf{D}$  can be obtained.

141 Then, this estimate is improved iteratively. It is not subjected to any scaling  
142 or other corrections. Details are documented by Siemes et al. (2013). This  
143 way of computing the linear trend is motivated by the fact that noise in an  
144 unconstrained model of the linear trend is substantially reduced as compared  
145 to that in unconstrained monthly solutions. Thus, a Wiener-type filter tai-  
146 lored for the linear trend is much less aggressive than those associated with  
147 monthly solutions. Therefore, the trend produced in this way as opposed  
148 to that derived from constrained monthly solutions shows a higher spatial  
149 resolution (Siemes et al., 2013).

150 For comparison, we produce another constrained estimate of the linear  
151 trend using CSR-RL05 monthly solutions and their noise covariance matrices  
152 with the same methodology. The CSR-RL05 solutions are complete to  
153 degree 96, whereas DMT-2 solutions extend to degree 120. To ensure a fair  
154 comparison of them, we additionally compute the linear trend in the case  
155 of DMT-2 to degree 96. This requires computing clones of DMT-2 monthly  
156 unconstrained solutions to degree 96. This does not necessarily require a re-  
157 processing of KBR data from scratch. These clones can be easily computed  
158 using DMT-2 unconstrained solutions and their noise covariance matrices.  
159 Technical aspects of these computations are provided in Appendix B. For  
160 brevity, we hereafter refer to the trend estimated from DMT-2 unconstrained  
161 solutions complete to degree 96 as “DMT-2-DEG-96”. Moreover, we compute  
162 models of the linear trend following the standard approach by first filtering  
163 the monthly solutions before the linear trend is estimated. To that end, we  
164 use CSR-RL05 monthly solutions subsequent to the DDK-5 and DDK-8 de-  
165 correlating non-isotropic filter (Kusche, 2007; Kusche et al., 2009). These

166 estimates of the linear trend are, hereafter, referred to as “CSR-RL05-DDK-  
167 5” and “CSR-RL05-DDK-8”, respectively. Their computation includes a  
168 co-estimation of a bias, as well as annual and semi-annual (co-) sinusoidal  
169 terms to be consistent with other estimates noted earlier. Given the fact that  
170 the DDK-8 filter in terms of the smoothing radius of an approximately equiv-  
171 alent Gaussian filter is smaller than the DDK-5 one (Kusche et al., 2009),  
172 an analysis of the results associated with these two filters allows the effect of  
173 the corresponding Gaussian smoothing radius to be studied in the side line.

### 174 *3.2. Results*

175 In this manuscript, we produce models of the linear trend in the time in-  
176 terval February 2003 – December 2008. This time interval is chosen since we  
177 compare results against, among others, surface elevations from ICESat laser  
178 altimeter data, which are available only to October 2009. Furthermore, a  
179 computation of GRACE-based linear trends with the Wiener filter of Siemes  
180 et al. (2013) requires dividing the time interval into multiple two-year seg-  
181 ments. Hence, currently we can compute the linear trend for either February  
182 2003 – December 2008 or February 2003 – December 2010. Only the former  
183 time interval allows for a consistent comparison of our results with those  
184 based on ICESat data.

185 In this section, we primarily focus on a comparison of the spherical har-  
186 monic models mentioned earlier, namely, DMT-2, “DMT-2-DEG-96”, CSR-  
187 RL05, “CSR-RL05-DDK-5”, and “CSR-RL05-DDK-8” (section 3.2.1). How-  
188 ever, to provide an idea on how spherical harmonic and mascons parametriza-  
189 tions compare, we close this section with a comparison between linear trends  
190 based on DMT-2 and GSFC\_global\_mascons\_v01 (section 3.2.2). The com-

191 putation of the linear trend in the latter case also includes a co-estimation  
192 of a bias, as well as annual and semi-annual (co-) sinusoidal terms to be  
193 consistent with the estimates based on DMT-2.

194 *3.2.1. Comparison with spherical harmonic models*

195 Figure 3 shows the five spherical harmonic linear trend estimates in the  
196 time interval February 2003 – December 2008 in terms of equivalent water  
197 heights (EWH).

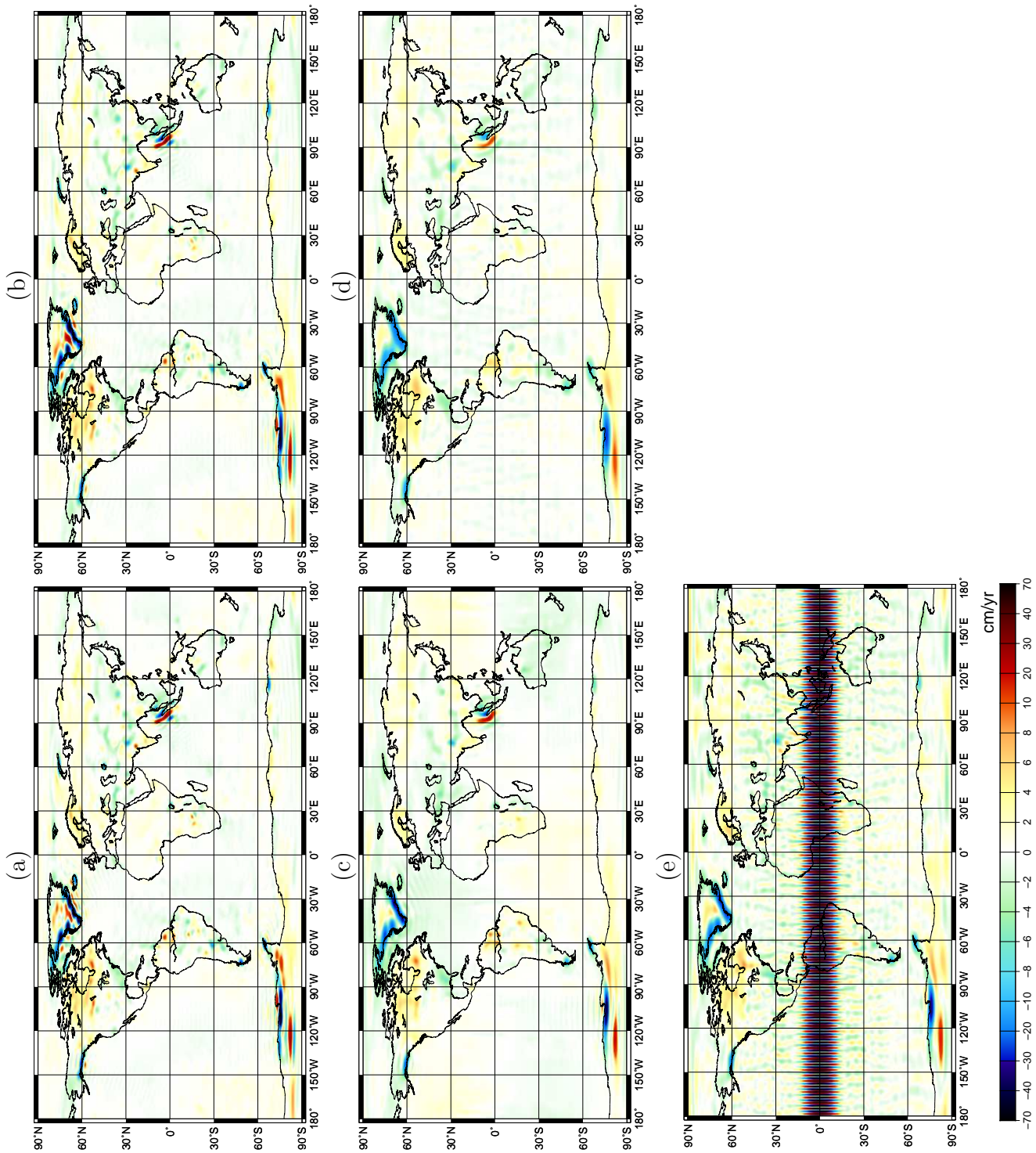


Figure 3: The linear trend computed in the time interval February 2003 – December 2008 in the cases of (a) DMT-2, (b) “DMT-2-DEG-96”, (c) CSR-RL05, (d) “CSR-RL05-DDK-8”, and (e) “CSR-RL05-DDK-8”. The maps are in terms of EWH. Their Root Mean Square (RMS) values are (a) 3.2 cm/yr, (b) 2.9 cm/yr, (c) 2.2 cm/yr, (d) 1.9 cm/yr, and (e) 2.4 cm/yr. Water heights bounded by latitudes  $\pm 10^\circ$  are excluded when computing RMS in the latter case.

198 The improved spatial resolution of Wiener filter estimates DMT-2, “DMT-  
199 2-DEG-96”, and CSR-RL05 compared to “CSR-RL05-DDK-5” is clearly vis-  
200 ible, particularly, in Greenland, Antarctica, and Gulf of Alaska. Moreover,  
201 the former two trend estimates show much more power compared to “CSR-  
202 RL05-DDK-5”. This is obvious when looking at the Root Mean Square  
203 (RMS) EWH, which are provided in the caption of Fig. 3. The situation is  
204 different when comparing the linear trend Wiener filter estimates with “CSR-  
205 RL05-DDK-8”. The latter also reveals an improved spatial resolution and  
206 increased signal power. However, “CSR-RL05-DDK-8” compromises results  
207 with stripes in equatorial areas bounded by latitudes  $\pm 10^\circ$  (Fig. 3e). This is  
208 the reason why those areas were excluded when calculating the RMS EWH  
209 in case of “CSR-RL05-DDK-8”. These results indicate that when comput-  
210 ing the linear trend from DDK-filtered monthly solutions, the filter variant,  
211 i.e., the corresponding Gaussian smoothing radius, needs to be chosen in line  
212 with the geographical area in interest. Further evidences to support this  
213 statement will be provided later.

214 A zoom-in at selected locations provides further insight into the differ-  
215 ences between the five linear trend estimates. To that end, we focus on two  
216 selected lakes (Section 3.2.1.1) and on the ice sheets (Section 3.2.1.2).

### 217 3.2.1.1 Lakes

218 We select two relatively small water bodies: Ladoga lake and the Aral sea.  
219 The five estimates of the linear trend over these areas are respectively pre-  
220 sented in Figs. 4 and 5. The trends produced from DMT-2 and its clone to  
221 degree 96 clearly demonstrate a gain of water mass in the Ladoga lake and a

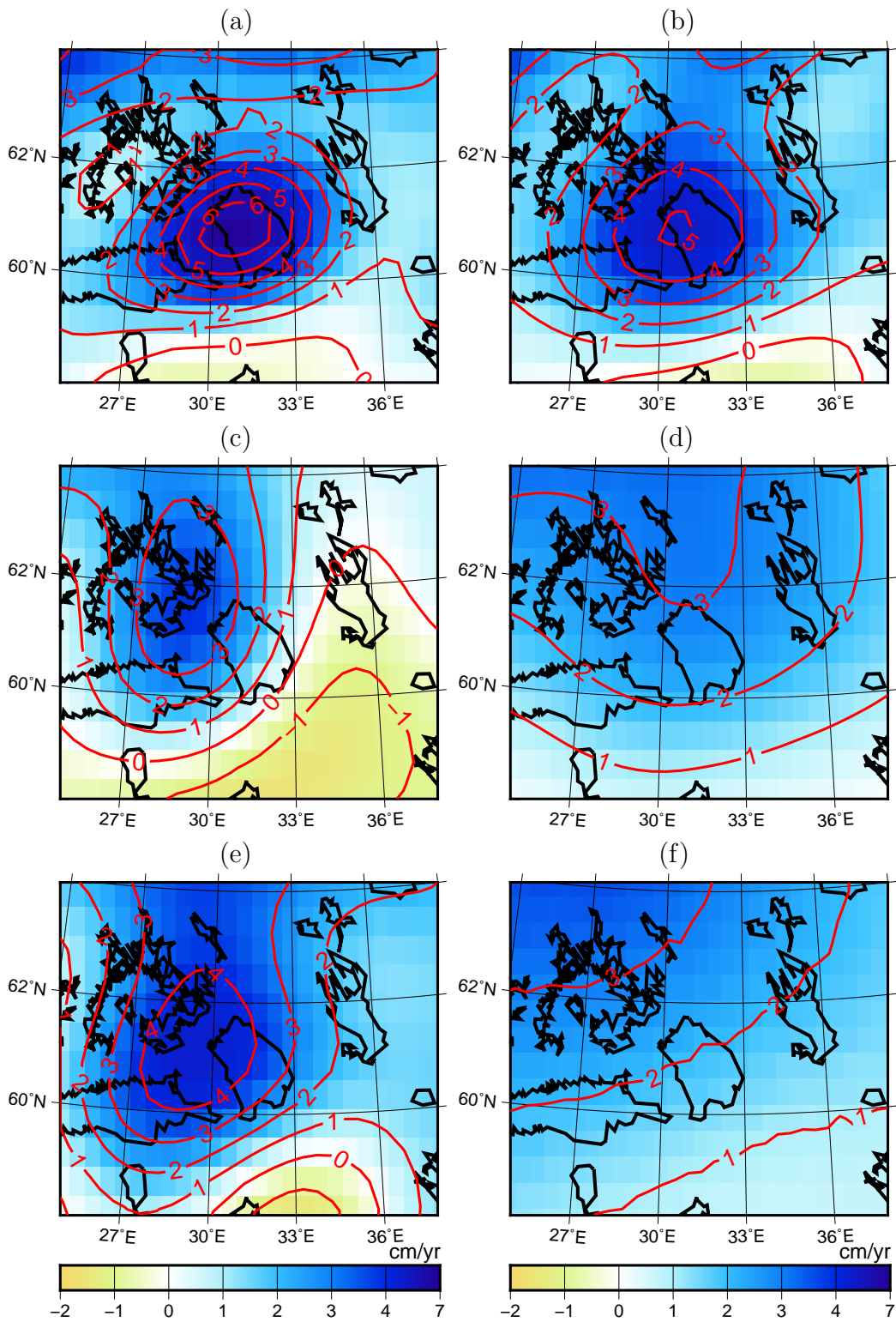


Figure 4: Linear trend in terms of EWH over the Ladoga lake computed in the time interval February 2003 – December 2008 from (a) DMT-2, (b) “DMT-2-DEG-96”, (c) CSR-RL05, (d) “CSR-RL05-DDK-5”, (e) “CSR-RL05-DDK-8”, and (f) GSFC\_global\_mascons\_v01.



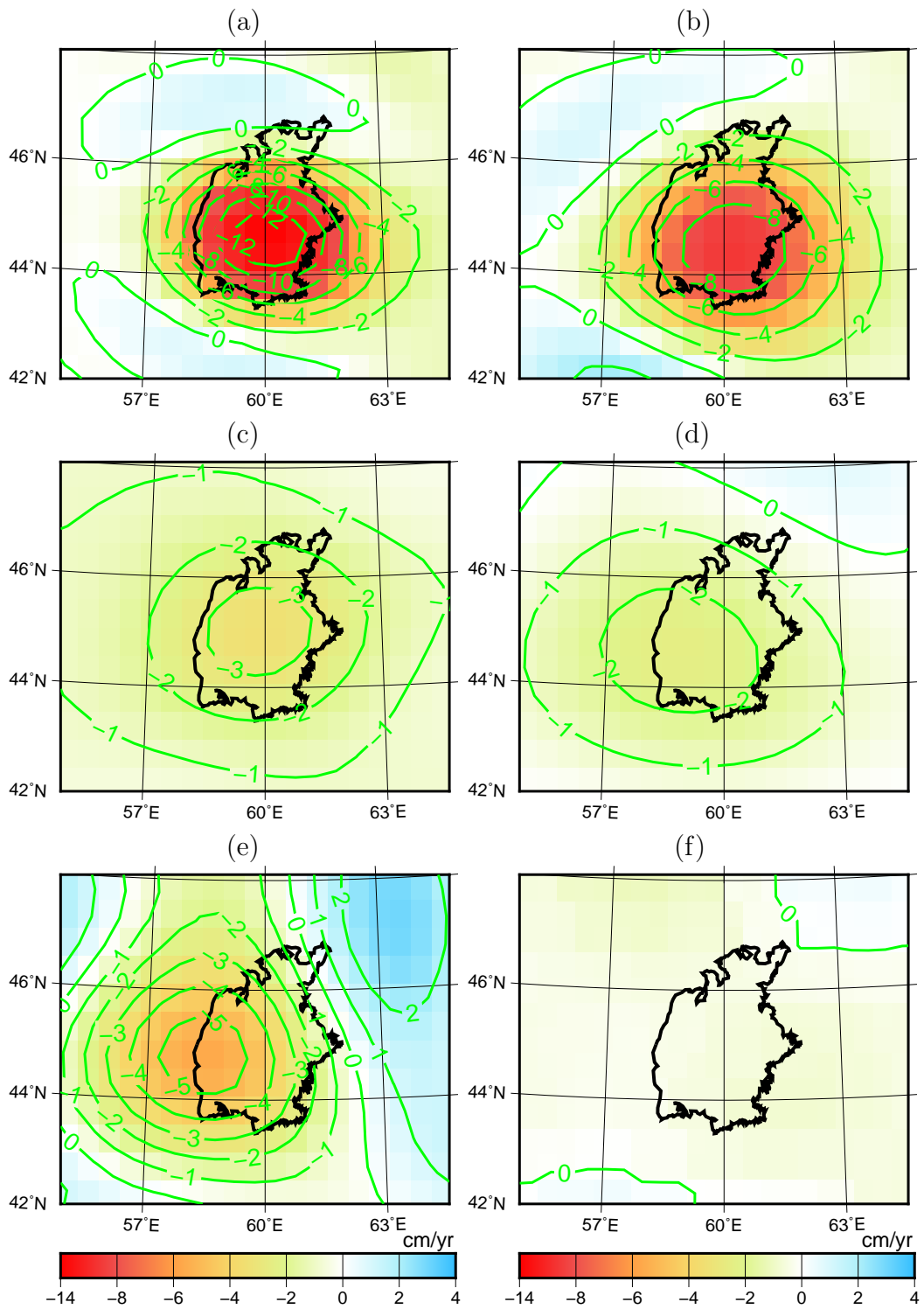


Figure 5: Linear trend in terms of EWH over the Aral sea computed in the time interval February 2003 – December 2008 from (a) DMT-2, (b) “DMT-2-DEG-96”, (c) CSR-RL05, (d) “CSR-RL05-DDK-5”, (e) “CSR-RL05-DDK-8”, and (f) GSFC\_global\_mascons\_v01.

222 loss of water mass in the Aral sea. Signal amplitudes are much larger in those  
223 cases compared to CSR-RL05, “CSR-RL05-DDK-5”, and “CSR-RL05-DDK-  
224 8”. In order to make an independent validation of the results, we consider  
225 water levels extracted from TOPEX/Poseidon and Jason-1 radar altimeter  
226 data over the period February 2003 – December 2008. From these mea-  
227 surements, we estimate linear trends together with a bias, as well as annual  
228 and semi-annual terms, to be consistent with the GRACE-derived estimates.  
229 Figure 6 shows the water height variations as a function of time and the  
230 computed mean linear trends over the Ladoga lake and Aral sea. A compar-  
231 ison with the GRACE-based estimates reveals that only DMT-2 provides a  
232 signal amplitude close to the radar altimeter-based estimates. The ampli-  
233 tude in case of “DMT-2-DEG-96” is reduced by about 20%. The estimates  
234 based on CSR-RL05, “CSR-RL05-DDK-5”, and “CSR-RL05-DDK-8” also  
235 show mass variations in both areas, but the signal is smeared over a much  
236 larger region and dramatically reduced. Correspondingly, linear trends are  
237 highly underestimated in those cases for both the Ladoga lake and the Aral  
238 sea. This is to be expected for “CSR-RL05-DDK-5” and “CSR-RL05-DDK-  
239 8”, because both lakes occupy a relatively small area (about 18000 km<sup>2</sup> in  
240 2004). The poor performance observed in case of CSR-RL05 is likely caused  
241 by an insufficiently accurate noise covariance matrix, which yields an inad-  
242 equate Wiener filter. We also notice that the peak mass variations are not  
243 centred on the target lakes in case of CSR-RL05, “CSR-RL05-DDK-5”, and  
244 “CSR-RL05-DDK-8” (an exception is CSR-RL05 for the Aral sea) unlike  
245 DMT-2 and “DMT-2-DEG96” (Figs. 4a and 5a). We additionally show in  
246 Fig. 7 the Aral sea region observed by the Landsat in summer months in 2003

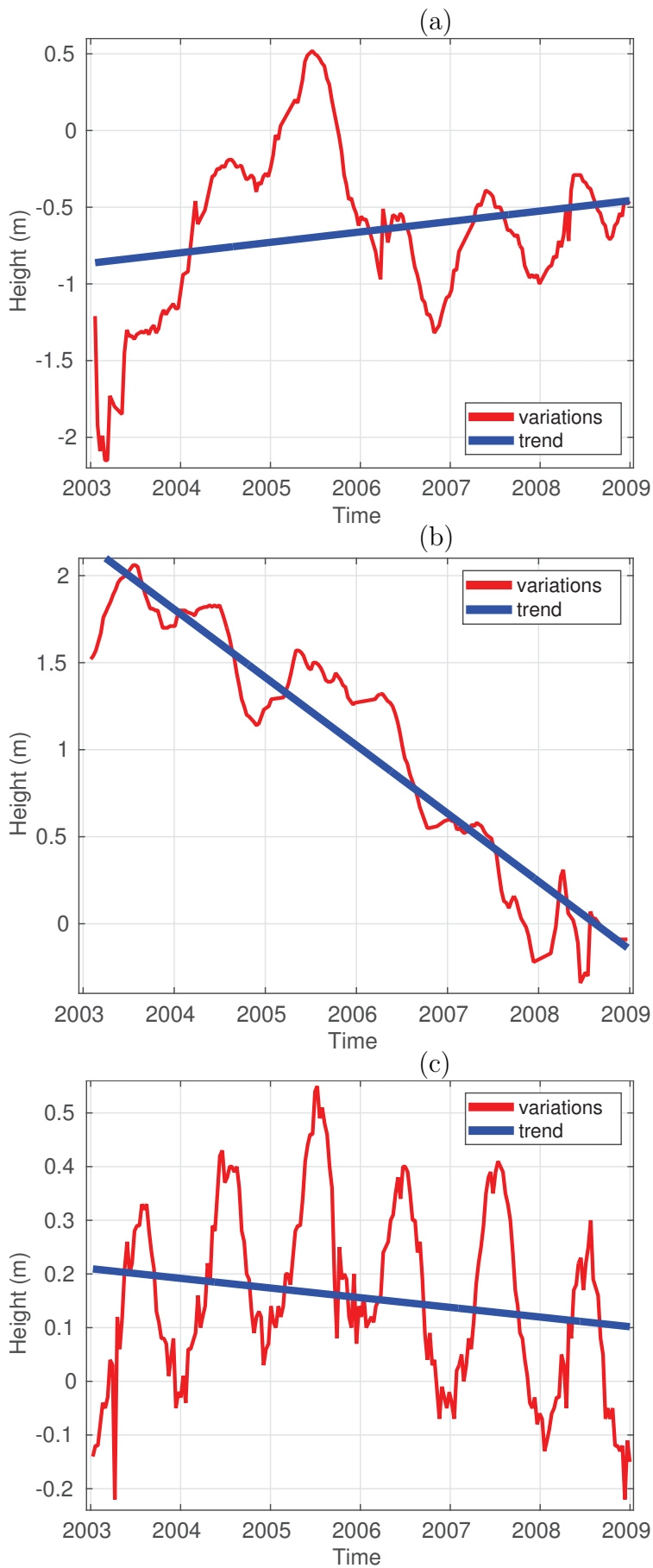


Figure 6: Water height variations and mean linear trend over (a) Ladoga lake, (b) Aral sea, and (c) Caspian sea in the time interval February 2003 – December 2008 from TOPEX/Poseidon and Jason-1 radar altimeter data. The mean linear trends are 6.92 cm/yr, -38.89 cm/yr, and -1.64 cm/yr for the Ladoga lake, Aral sea, and Caspian sea, respectively.

247 – 2008. This time interval corresponds to that for which the linear trend is  
248 computed. Summer months are chosen because they offered a clear sky. The  
249 figure reveals the presence of a massive water loss. This loss is primarily  
250 pronounced in the main water body, i.e., the one centred in the exhibited  
251 Landsat pictures. The radar altimeter data exploited in Fig. 6b are collected  
252 just over this water body, too.

253 Finally, a comparison between “CSR-RL05-DDK-5” and “CSR-RL05-  
254 DDK-8” (Fig. 4d versus Fig. 4e and Fig. 5d versus Fig. 5e) clearly reveals  
255 an improved spatial resolution when choosing a smaller DDK filter. At the  
256 same time, stripes are barely present in case of “CSR-RL05-DDK-8” esti-  
257 mates. Nevertheless, even a small DDK filter could not lead to a spatial  
258 resolution achievable with the Wiener filter.

### 259 *3.2.1.2 Ice sheets*

260 We compare the five spherical harmonic estimates of the linear trend over  
261 the Greenland and Antarctica. The linear trend estimates in EWH in the  
262 time interval February 2003 – December 2008 are shown over Greenland and  
263 Antarctica in Figs. 8 and 9, respectively. The linear trends in physical height  
264 changes acquired from ICESat laser altimeter data in the same time interval  
265 are provided in Figs. 8f and 9f. These ICESat-based trends are computed  
266 using the overlapping footprint approach described in (Felikson et al., 2016)  
267 and (Gunter et al., 2014) for Greenland and Antarctica, respectively. In both  
268 cases, they have a spatial resolution of about 20 km. We smooth them with  
269 a 75 km (half-width) Gaussian filter (Jekeli, 1981) to facilitate a comparison  
270 of them with the GRACE-based estimates (Figs. 8g and 9g).

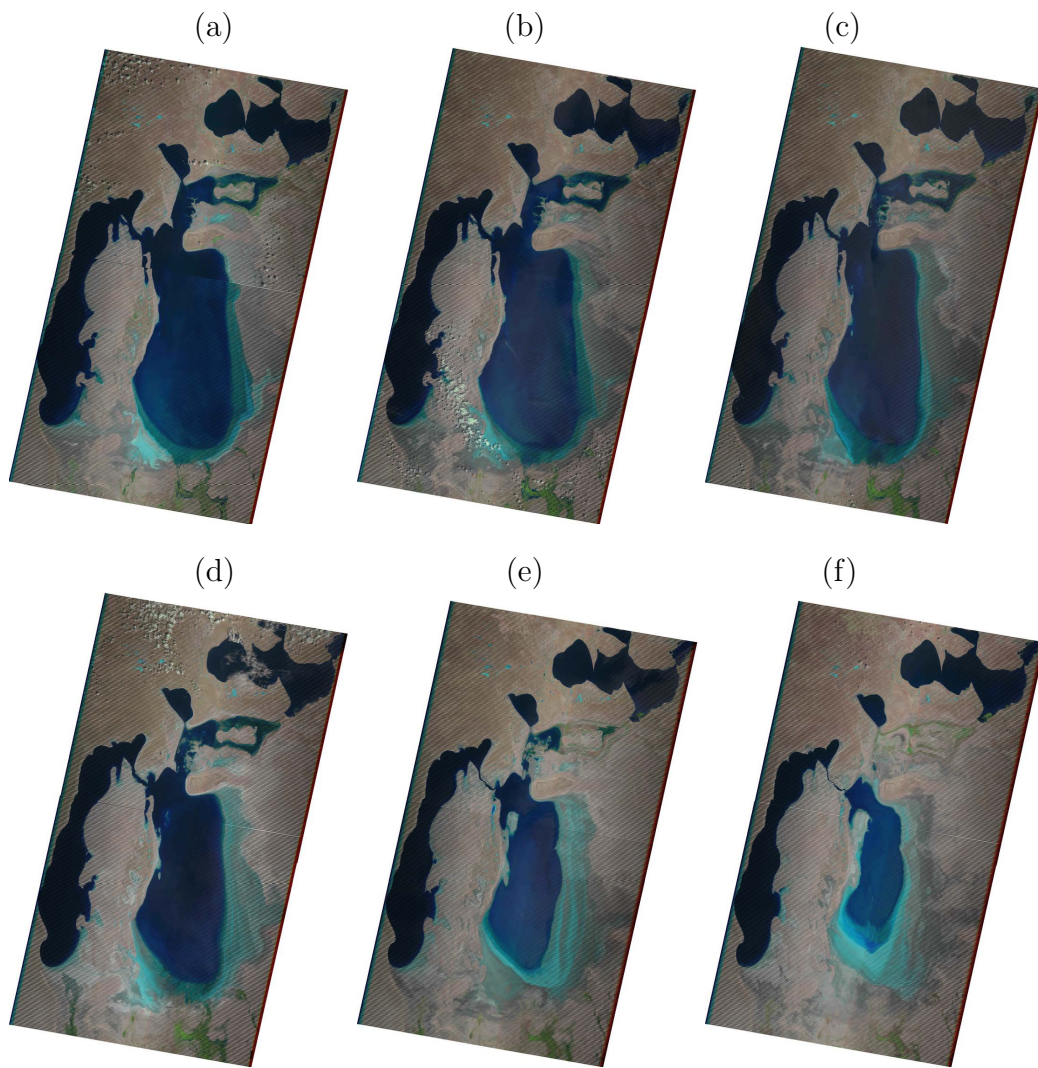


Figure 7: Aral sea region observed by Landsat in 2003 (a) – 2008 (f) in summer months.

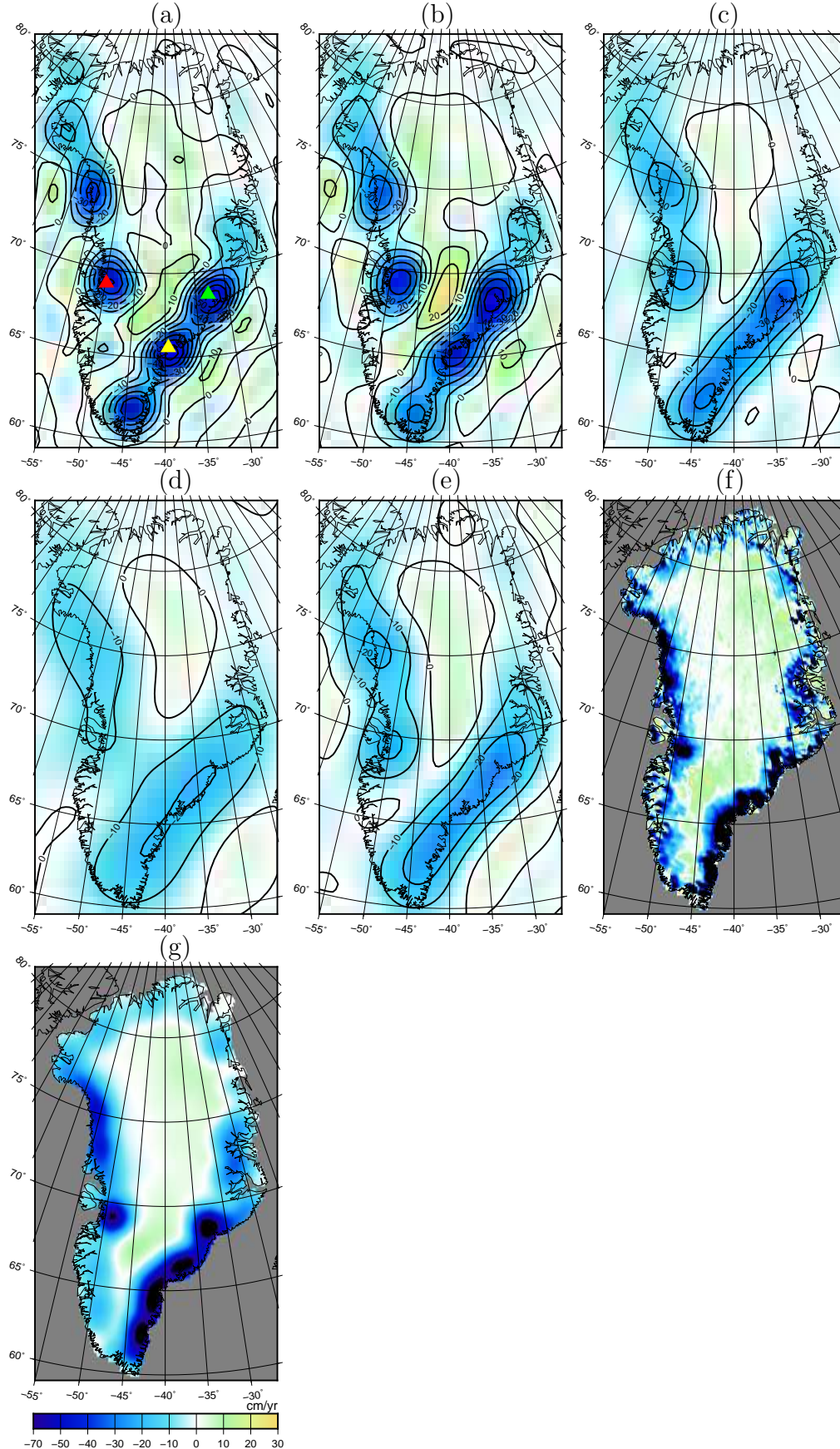


Figure 8: Linear trend over Greenland computed in the time interval February 2003 – December 2008 from (a) DMT-2, (b) “DMT-2-DEG-96”, (c) CSR-RL05, (d) “CSR-RL05-DDK-5”, and (e) “CSR-RL05-DDK-8” as well as ICESat data (f) without and (g) with a 75 km (half-width) Gaussian smoothing. The GRACE-based estimates are in EWH, whereas those based on ICESat are in physical heights. The location of Jakobshavn and Kangerdlugssuaq glaciers are marked in the top left picture with red and green triangles, respectively. The average location of Helheim, Ikertivaq, and Koge Bugt glaciers is marked in the same picture with a yellow triangle.



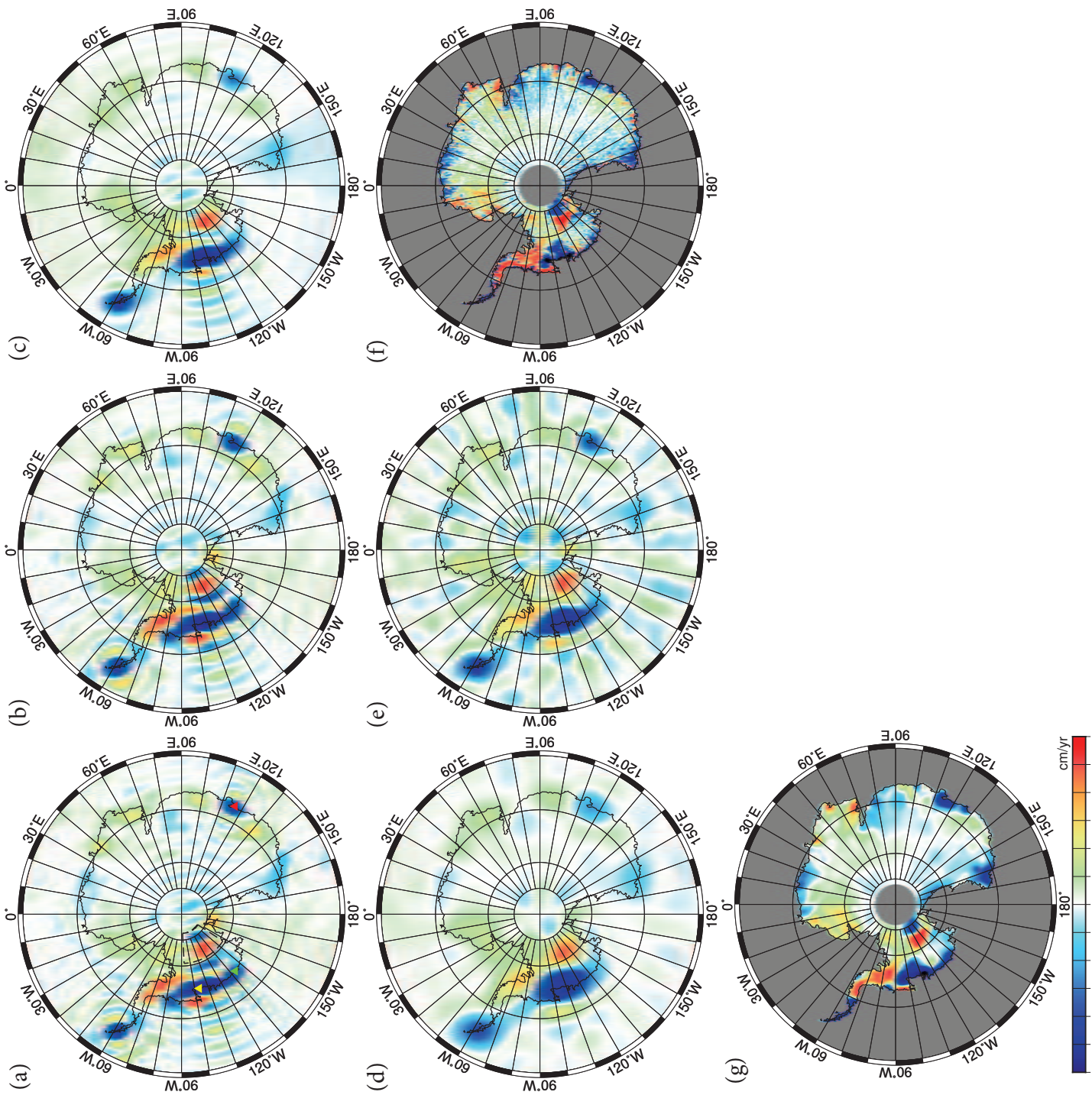


Figure 9: Same as Fig. 8, but for Antarctica. The location of Totten glacier is marked in the top left picture with a red triangle. The average location of Pine Island and Thwaites glaciers as well as that of Getz Ice Shelf and Land Glacier are marked in the same picture with yellow and green triangles. The selected area in West Antarctica is marked with a dashed, black box.

271 One can see from Figs. 8 and 9 that DMT-2 and its clone computed to  
272 degree 96 have the highest spatial resolution allowing for a clear distinction  
273 of signals related to individual glaciers. For instance, signals associated with  
274 the Jakobshavn and Kangerdlugssuaq glaciers, as well as those related to the  
275 combination of Helheim, Ikertivaq, and Koge Bugt glaciers can be clearly seen  
276 in Greenland. We also want to point to the good agreement of trend patters  
277 over Antarctica from DMT-2 and “DMT-2-DEG-96” with results based on  
278 the ICESat data. Examples are signals associated with (i) Totten glacier  
279 in East Antarctica, (ii) the combined signal of Pine Island and Thwaites  
280 glaciers, and (iii) the combined signal of Getz Ice shelf and Land glacier  
281 in West Antarctica. Another notable example is the area near the pole in  
282 West Antarctica that is marked by a dashed, black box in Fig. 9a. We zoom  
283 in on this region in Fig. 10. DMT-2, “DMT-2-DEG-96”, and ICESat data  
284 consistently reveal a positive and a negative anomaly there located close to  
285 each other. The positive anomaly there is most likely associated with an  
286 accumulation of ice, which is in accordance with some earlier findings (e.g.,  
287 Joughin and Tulaczyk, 2002). Though the CSR-RL05 Wiener filter estimate  
288 and its DDK filter variants reveal a similar pattern, the signal amplitude  
289 retrieved is somewhat reduced.

290 At the same time we admit that linear trends from DMT-2 and “DMT-2-  
291 DEG-96” suffer from some high-frequency errors. They show up in the form  
292 of ringing artifacts in the vicinity of locations with strong mass variations.  
293 For instance, in Greenland, they are as large as about 12% of the signal. We  
294 consider them as noise given the fact that they are present not only over the  
295 ice sheets, but also over the oceans, where mass variations are expected to be



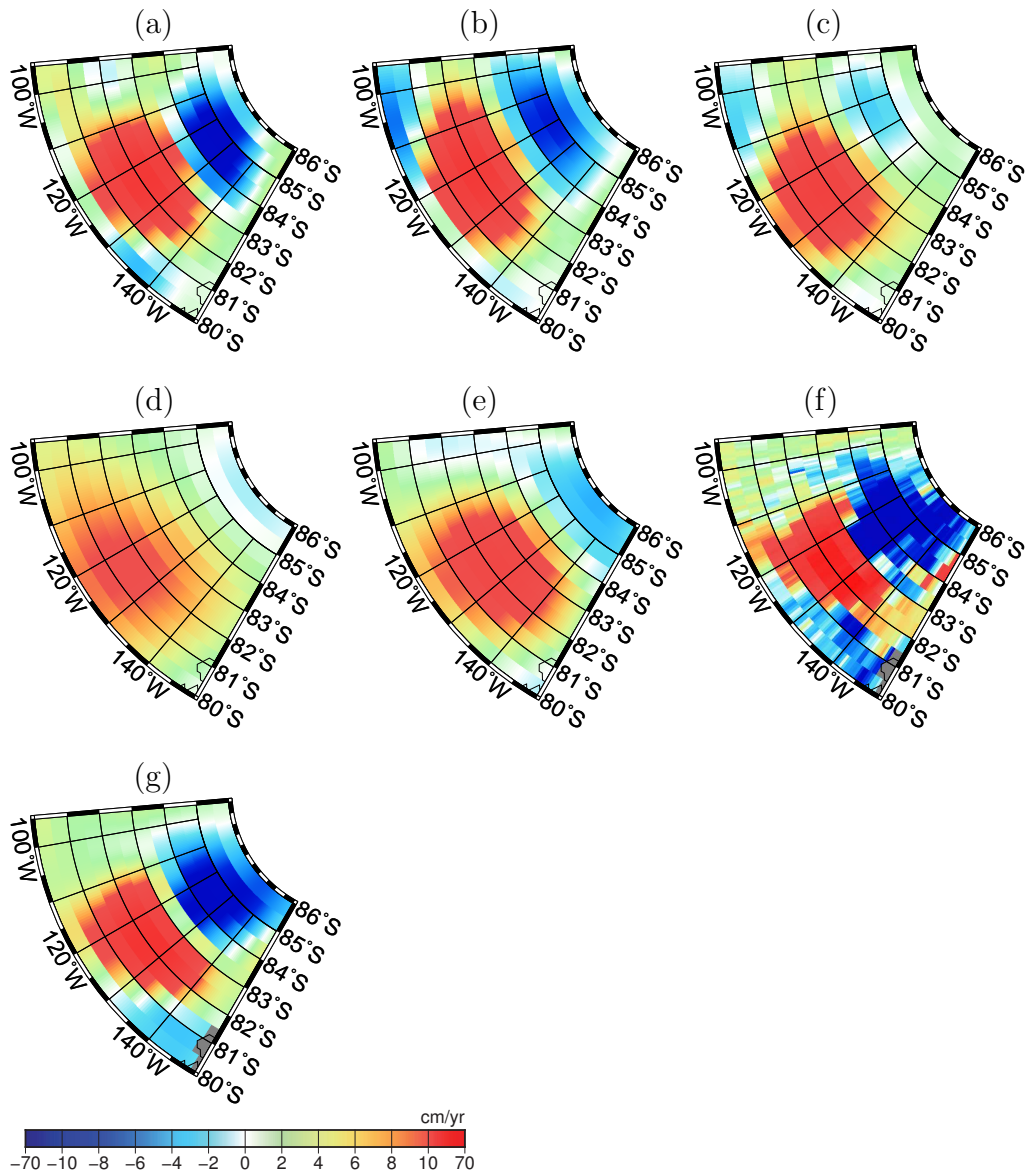


Figure 10: Linear trends over the selected area in West Antarctica, marked with a dashed black box in Fig. 9a. They are computed in the time interval February 2003 – December 2008 from (a) DMT-2, (b) “DMT-2-DEG-96”, (c) CSR-RL05, (d) “CSR-RL05-DDK-5”, and (e) “CSR-RL05-DDK-8” as well as ICESat data (f) without and (g) with a 75 km (half-width) Gaussian smoothing. The GRACE-based estimates are in EWH, whereas those based on ICESat are in physical heights.

296 minor, if not zero. The likely origin of this phenomenon is an abrupt signal  
297 truncation in the frequency domain at the maximum degree (degree 120 and  
298 96, respectively). The best way to solve this problem is still a topic of active  
299 research.

300 The DDK-filtered linear trend estimates do not offer the spatial resolution  
301 achieved in cases of DMT-2 or its clone to degree 96. “CSR-RL05-DDK-8”  
302 as compared to “CSR-RL05-DDK-5” reveals a higher spatial resolution in  
303 both Greenland and Antarctica. Results related to “CSR-RL05-DDK-8” in  
304 Antarctica are somewhat polluted with stripes. In Greenland, however, no  
305 sign of stripes is present. This means that a further improvement of spatial  
306 resolution could be achieved there when using a smaller DDK filter than the  
307 DDK-8 one.

308 Furthermore, we validate the GRACE models over the Antarctica quan-  
309 titatively by comparing the results to those derived from laser altimetry  
310 (Gunter et al., 2009). To that end, we transform the ICESat-based linear  
311 trend estimate from physical heights into EWH in line with the methodology  
312 described by Gunter et al. (2014). This approach takes into account sur-  
313 face mass changes from the regional atmospheric climate model RACMO2  
314 (Lenaerts et al., 2012) and the accompanying firn densification model (Ligten-  
315 berg et al., 2011) as well as the Glacial Isostatic Adjustment model of White-  
316 house et al. (2012). Figure 11 exhibits RMS reductions of the ICESat-  
317 based linear trend EWH by the GRACE-based ones in percentages, i.e.,  
318  $100 \times \left( \frac{\text{RMS}_{\text{ICESat}} - \text{RMS}_{\text{ICESat-GRACE}}}{\text{RMS}_{\text{ICESat}}} \right)$ , subsequent to a Gaussian smoothing of the  
319 ICESat-based results at different widths. For computing the RMS reduction  
320 in percent, the entire ice sheet is seen as a time series. This comparison

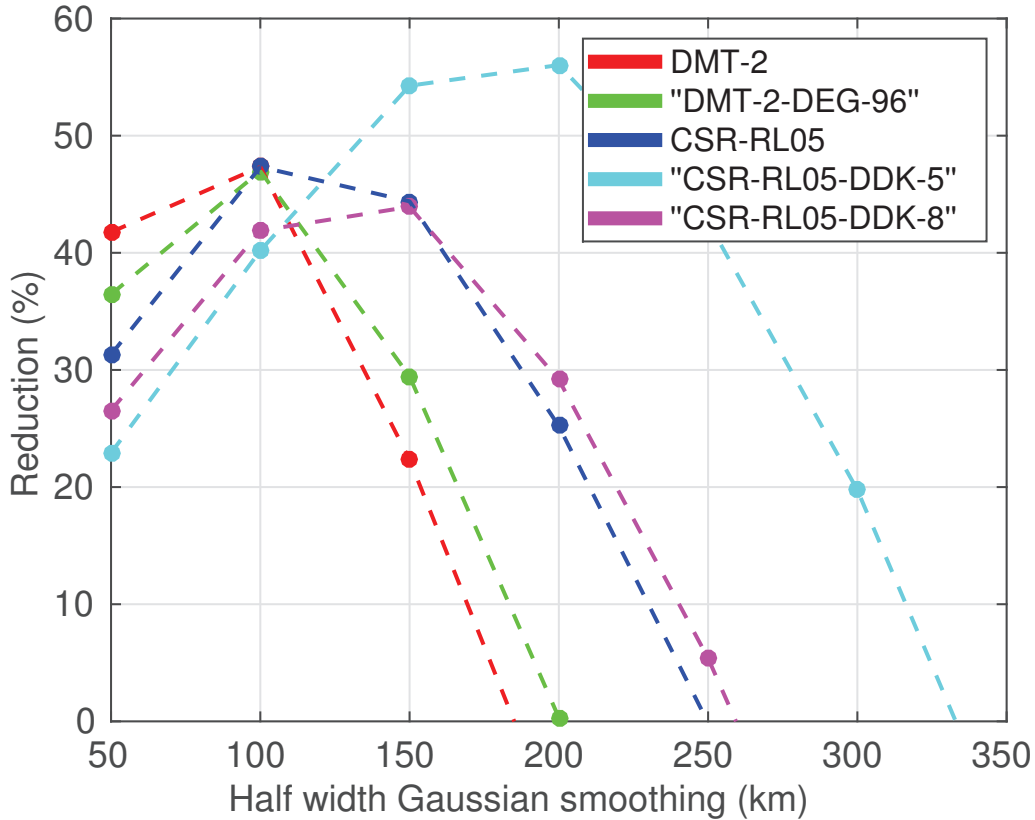


Figure 11: The RMS signal reductions (in percentages) of the ICESat-based linear trend EWH by the GRACE-based ones, i.e.,  $100 \times \left( \frac{\text{RMS}_{\text{ICESat}} - \text{RMS}_{\text{ICESat-GRACE}}}{\text{RMS}_{\text{ICESat}}} \right)$ , subsequent to the Gaussian smoothing of the ICESat-based results at different widths over Antarctica.

321 considers both the spatial pattern as well as the magnitude of the signal.  
 322 The Gaussian smoothing of the ICESat-based results is performed at dif-  
 323 ferent widths and compared to the GRACE-derived trend to approximately  
 324 determine the spatial resolution of the GRACE. The peaks in Fig. 11 are  
 325 interpreted as the spatial resolution of the respective GRACE solution in  
 326 terms of the Gaussian smoothing filter. Compared to CSR-RL05, the com-  
 327 puted signal reductions are slightly larger for DMT-2 and “DMT-2-DEG-96”

328 at spatial scales smaller than about 100 km (half-width). The opposite is ob-  
329 served at larger spatial scales. We interpret this observation as an evidence  
330 that the spatial resolution of the DMT-2 model and its clone is higher. To  
331 understand this behaviour, we emphasize that only the ICESat-based results  
332 are subject to the Gaussian smoothing. Hence, the spatial resolution of those  
333 results reduces as the spatial scale increases. Consequently, for GRACE es-  
334 timates with higher spatial resolution, the peak in their signal reductions of  
335 the ICESat-based EWH occurs at smaller smoothing radii.

336 Furthermore, it is worth noting that the signal reductions in the case of  
337 the CSR-RL05 Wiener filter estimate are much higher than in case of the  
338 DDK-filtered ones at spatial scales smaller than 100 – 150 km (half-width).  
339 We interpret this as a consequence of a higher spatial resolution of the Wiener  
340 filter compared to the DDK filters. This is also supported by the maps shown  
341 in Figs. 8, 9, and 10.

342 On the other hand, as it can be seen from Fig. 9, the higher the spatial  
343 resolution of a GRACE solution, the higher its noise content. The ringing  
344 artifacts can be clearly seen for the Wiener filter estimates in Fig. 9 and they  
345 are also reflected in the lower values of RMS reduction for these solutions  
346 compared to the DDK-filtered estimates at relatively large spatial scales.

347 Finally, it is important to note that DMT-2 as compared to its clone com-  
348 puted to degree 96 reveals a slightly better agreement with the ICESat-based  
349 estimates at spatial scales smaller than 100–150 km (half-width). However,  
350 it should be noted that this must be almost entirely attributed to a higher  
351 maximum degree considered at the filtering stage and not to information  
352 content of KBR data (Farahani, 2013).

353 *3.2.2. A preliminary comparison with a mascon parametrization*

354 Figure 12 shows the linear trends estimated based on the DMT-2 spheri-  
355 cal harmonic (to degree 120) and GSFC\_global\_mascons\_v01 mascon models  
356 in the time interval February 2003 – December 2008 in terms of EWH at  
357 the global scale. The color scale is intentionally saturated in order to re-  
358 veal model differences more clearly. Both models demonstrate a high spatial  
359 resolution. This is, in particular, notable in areas where substantial mass  
360 variations occur, e.g., Antarctica, Greenland, Gulf of Alaska, Iceland, Cana-  
361 dian Arctic archipelago, Novaya Zemlya archipelago, and Svalbard (Spitsber-  
362 gen) archipelago. DMT-2 and GSFC\_global\_mascons\_v01 both demonstrate  
363 a high concentration of the signal along the coast in these areas. This is  
364 typically expected in the case of mascon models due to a priori information  
365 imposed, for instance, by defining the mascon geometry consistently with  
366 coast lines. We find this, however, remarkable in the case of DMT-2 in view  
367 of the fact that no such a priori information is imposed.

368 DMT-2 as compared to GSFC\_global\_mascons\_v01 suffers from somewhat  
369 larger inaccuracies in the so-called “quite areas”, i.e., areas void of substantial  
370 temporal gravity field variations (e.g., oceans and deserts), which is partly  
371 explained by the presence of the previously noted ringing artifacts. Finding  
372 the best way to suppress those inaccuracies will be the subject of a future  
373 research. This, for instance, could be done by additional filtering of spherical  
374 harmonic coefficients by preventing the signal variances (i.e., diagonal ele-  
375 ments in matrix  $\mathbf{D}$ ) in “quite areas” from exceeding a predefined threshold.

376 Finally, one can identify numerous differences between the DMT-2 and  
377 GSFC\_global\_mascons\_v01 models at small spatial scales. Examples are Lake

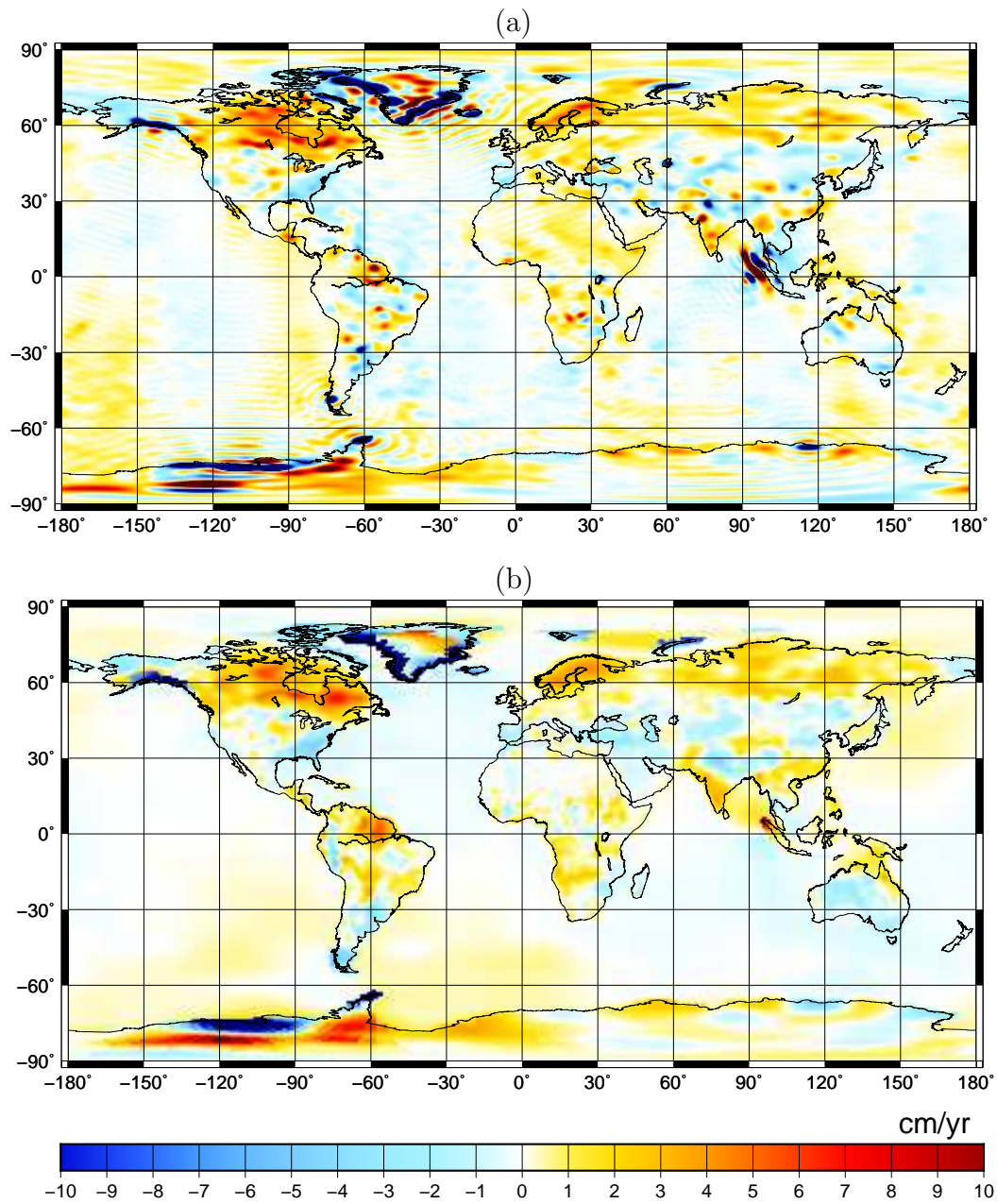


Figure 12: The linear trend computed in the time interval February 2003 – December 2008 in the cases of (a) DMT-2 and (b) GSFC\_global\_mascons.v01. The maps are in terms of EWH. Their RMS values are (a) 3.19 cm/yr and (b) 1.58 cm/yr. The Color scale is intentionally saturated.

378 Victoria, Ladoga lake, Aral sea, Caspian sea, Amazon river basin, and Patag-  
379 onia. A comprehensive analysis of such differences demands a separate re-  
380 search, which we postpone to a later stage. Here, we limit ourselves to only  
381 three water bodies: Aral sea, Ladoga lake, and Caspian sea. In Ladoga  
382 lake and Aral sea, GSFC\_global\_mascons\_v01, unlike DMT-2, fails to cap-  
383 ture respective water gain and water loss signals (see Fig. 4a versus Fig. 4f  
384 and Fig. 5a versus Fig. 5f as well as Fig. 6a and Fig. 6b). On the contrary,  
385 GSFC\_global\_mascons\_v01 reveals the water loss in the Caspian sea. DMT-  
386 2 fails in that respect and, by the way, so do all other spherical harmonic  
387 models considered in our manuscript (cf. Fig. 3c – Fig. 3e). The reason for  
388 this is yet to be investigated. It is worth noting that the loss of water in the  
389 Caspian sea in the time interval under consideration is captured by radar  
390 altimetry data, too (cf. Fig. 6c).

#### 391 **4. Conclusions**

392 We computed new estimates of the long-term linear trend in mass re-  
393 distribution based on the DMT-2 model, which comprises monthly gravity  
394 field solutions and corresponding full noise covariance matrices complete to  
395 spherical harmonic degree 120. A novel feature of the DMT-2 model is the  
396 accurate computation and incorporation of stochastic properties of coloured  
397 noise when processing KBR data, which also accounts for gradual variations  
398 of the noise characteristics in time. This ensures a statistically optimal inver-  
399 sion of KBR data, and more importantly, an accurate computation of noise  
400 covariance matrices of monthly solutions. These matrices play a key role in  
401 the design of Wiener-type filters, including that proposed by Siemes et al.

402 (2013) for estimating the linear trend. For comparison, we produced esti-  
403 mates of the linear trend from CSR-RL05 monthly solutions and their noise  
404 covariance matrices using the same methodology to build the linear trend  
405 Wiener filter. The linear trend estimate based on DMT-2 demonstrates a  
406 higher spatial resolution, even if we lower the maximum degree in the DMT-  
407 2 model to degree 96 to be consistent with the CSR-RL05 model. It allows  
408 for a clear detection of mass variation signals in relatively small water bodies  
409 and individual outlet glaciers of the ice sheets. Moreover, it shows a much  
410 better fit to actual water level and surface elevation variations extracted  
411 from radar and laser altimeter data. We attribute the higher spatial resolu-  
412 tion of the DMT-2 linear trend estimates compared to that estimated from  
413 CSR-RL05 to an accurate computation of monthly noise covariance matri-  
414 ces, which was possible due to a proper handling of coloured noise in KBR  
415 data. However, there is still space for further improvements. The linear trend  
416 estimates based on DMT-2 or its clone computed to degree 96 suffer from  
417 some high-frequency inaccuracies. Those inaccuracies manifest themselves  
418 in the form of ringing artifacts in the vicinity of locations with strong mass  
419 variations. The best way to deal with this problem is still under investiga-  
420 tion. The estimates of the linear trend obtained from DMT-2 are publicly  
421 available for download.<sup>1,2</sup> The linear trend models analysed and presented  
422 in this manuscript are related to a six-year time interval (February 2003 –  
423 December 2008). Similar models for longer time intervals are to be produced  
424 and released subsequently.

---

<sup>1</sup>[www.citg.tudelft.nl](http://www.citg.tudelft.nl)

<sup>2</sup>[www.researchgate.net/profile/Hassan.H.Farahani](http://www.researchgate.net/profile/Hassan.H.Farahani)



425 Furthermore, we produced additional variants of the linear trend with a  
426 commonly-used approach: from CSR-RL05 monthly solutions subject to the  
427 DDK-5 and DDK-8 de-correlating non-isotropic filters. As compared to the  
428 Wiener filters, these variants showed a reduced spatial resolution and signal  
429 power. In a comparison with the altimetry-based results over Antarctica,  
430 the linear trends obtained in this way showed peak spatial resolutions about  
431 twice (in case of DDK-5 filtering) and 1.5 times (in case of DDK-8 filtering) as  
432 coarse as those after the Wiener filtering. Thus, the DDK-8 filtering showed a  
433 notably higher spatial resolution than the DDK-5 filtering. Near the equator,  
434 nevertheless, the DDK-8-filtered results showed strong stripes. This implies  
435 that a smaller DDK filter cannot be successfully applied uniformly over the  
436 entire globe. We conclude that when estimating the linear trend based on  
437 DDK-filtered time series of solutions, one needs to choose different DDK  
438 filters for different geographical areas.

439 A comparison of DMT-2 with GSFC\_global\_mascons\_v01, a recent global  
440 mascon model, suggests that both models demonstrate a high spatial res-  
441 olution in areas known for substantial temporal gravity field changes (e.g.,  
442 Antarctica, Greenland, Gulf of Alaska, Iceland, Canadian Arctic archipelago,  
443 Novaya Zemlya archipelago, and Svalbard archipelago). DMT-2 compared  
444 to GSFC\_global\_mascons\_v01 showed somewhat larger inaccuracies in areas  
445 known for minor mass variations (e.g., ocean and deserts). The absence of  
446 such inaccuracies in GSFC\_global\_mascons\_v01 is explained by a priori infor-  
447 mation typically imposed in such areas, for instance, by defining the mascon  
448 geometry consistently with coast lines (e.g., Watkins et al., 2015). Such a  
449 priori information was never used when computing DMT-2. To the knowl-

450 edge of authors, they are absent in all spherical harmonic models produced  
451 so far. An incorporation of such a priori information in the production of  
452 future spherical harmonic models could be the subject of future research en-  
453 deavours. This could be incorporated at the a posteriori stage, i.e., when  
454 filtering spherical harmonic coefficients. More specifically, this could be done  
455 by predefining and enforcing relatively small signal variances in areas with  
456 minor mass variations when building and applying a Wiener-type filter. Fi-  
457 nally, the comparison revealed numerous differences between DMT-2 and  
458 GSFC\_global\_mascons\_v01 at small spacial scales. A verification of a few of  
459 those features, namely, in Ladoga lake, Aral sea, and Caspian sea, led to  
460 mixed conclusions in favour of either model in each instance. An in-depth  
461 comparison of other small scale differences is postponed to further publi-  
462 cations. It is worth noting that spherical harmonic and mascon models use  
463 vastly different parametrizations. That is, they belong to two vastly different  
464 classes of time-varying gravity field models. Hence, an in-depth comparison  
465 of them deserves a separate research in any way.

## 466 **Acknowledgments**

467 The research was financially supported by the Nederlandse organisatie  
468 voor Wetenschappelijk Onderzoek (Netherlands Organization for Scientific  
469 Research, NWO). High-performance computing facilities were provided by  
470 the Stichting Nationale Computerfaciliteiten (National Computing Facilities  
471 Foundation, NCF). GRACE level-1B data were provided by the Jet Propul-  
472 sion Laboratory (JPL). The CSR-RL05 unconstrained monthly solutions as  
473 well as those constrained by the DDK-5 and DDK-8 filters were provided by

474 the International Centre for Global Earth Models (ICGEM). The CSR-RL05  
475 monthly noise covariance matrices were provided by the Center for Space Re-  
476 search (CSR) at the University of Texas at Austin. Landsat pictures as well  
477 as TOPEX/Poseidon and Jason-1 radar altimeter data were made available  
478 by the US Geological Survey (USGS) and the US Department of Agriculture  
479 (USDA), respectively. GSFC\_global\_mascons\_v01 was provided by Goddard  
480 Space Flight Center (GSFC). These supports are gratefully acknowledged.  
481 We are thankful to Natthachet Tangdamrongsub for an assistance in com-  
482 piling the Landsat pictures. We thank the editor, Volker Klemann, and two  
483 anonymous reviewers for their constructive remarks and corrections, which  
484 helped us to improve the quality of the manuscript.

## 485 **Appendix A. Residual data**

DMT-2 like its predecessor DMT-1 used a variant of the acceleration approach. So-called “range combinations” were obtained from bias-corrected inter-satellite ranges at three successive epochs with a three-point double differentiation scheme (Liu, 2008; Liu et al., 2010)

$$\bar{a}(t) = \frac{\mathbf{e}(t - \Delta t) \cdot \mathbf{e}(t) \rho(t - \Delta t) - 2\rho(t)}{(\Delta t)^2} + \frac{\mathbf{e}(t) \cdot \mathbf{e}(t + \Delta t) \rho(t + \Delta t)}{(\Delta t)^2}, \quad (\text{A.1})$$

486 with  $\Delta t$  the sampling rate,  $\rho(t)$  the bias-corrected inter-satellite ranges, and  
487  $\mathbf{e}(t)$  the line-of-sight unit vectors pointing from the trailing to the leading  
488 satellite, and  $t$  the measurement epoch. It is, in essence, similar to a scheme  
489 developed earlier by Ditmar and van Eck van der Sluijs (2004) and Ditmar

490 et al. (2006) to determine the Earth’s gravity field from kinematic orbits of  
491 low Earth orbiters.

492 To reduce KBR data into residual range combinations, the following back-  
493 ground force models were used:

- 494 (i) Static gravity field with DGM-1S (Farahani et al., 2013a,b).
- 495 (ii) Third-body perturbations from the JPL DE405/LE405 lunar and plan-  
496 etary ephemerides (Standish, 1998).
- 497 (iii) Solid Earth and pole tides in line with the 2003 conventions of the  
498 International Earth Rotation and Reference Systems Service (IERS)  
499 (McCarthy and Petit, 2004).
- 500 (iv) Ocean tides according to EOT11a to spherical harmonic degree 80 (Sav-  
501 cenko et al., 2012).
- 502 (v) Non-tidal atmospheric and oceanic variations from the fifth release of  
503 the Atmosphere and Ocean De-aliasing level-1b (AOD1B) product to  
504 spherical harmonic degree 100 (Dobslaw et al., 2013).
- 505 (vi) Ocean pole tide defined by the model of Desai (2002) to spherical har-  
506 monic degree 30.
- 507 (vii) General relativity corrections in line with the IERS 2003 conventions  
508 (McCarthy and Petit, 2004).
- 509 (viii) Non-gravitational perturbations from the second release of GRACE ac-  
510 celerometer and attitude data, which are provided as a part of GRACE  
511 level-1B data (Case et al., 2004).

512 Additionally, the background force models were iteratively improved. The  
513 production of the monthly solutions involved three iterations, in all of which

514 the gravity field retrieval was performed to degree 120. The first two itera-  
515 tions were executed in line with Liu et al. (2010). That is, the unconstrained  
516 solutions computed at a given iteration were truncated at degree 13 and in-  
517 cluded into the list of background force models used in the next iteration.  
518 In the third iteration, the solutions of the previous iteration were treated  
519 differently. Instead of a truncation, they were processed by applying the  
520 Wiener-type filter (Klees et al., 2008b). They were then included into the  
521 list of the background force models to obtain the unconstrained solutions at  
522 the third (i.e., final) iteration. The GRACE satellites in several time inter-  
523 vals, namely, September – October 2004, November – December 2009, and  
524 January – February 2010, followed an orbit with a relatively short repeat pe-  
525 riod. This leads to relatively high inaccuracies in the unconstrained solutions  
526 for these months (e.g., Farahani et al., 2014). These inaccuracies occur in the  
527 entire range of degrees, including those below degree 13. Thus, performing  
528 the second iteration as described above would not lead to optimal results.  
529 Hence, DMT-2 solutions for these months were computed by performing the  
530 second iteration in the same manner as the third one, so that noise in un-  
531 constrained solutions, however large, was efficiently suppressed in the entire  
532 range of degrees.

533 The background force models entered a dynamic orbit computation in  
534 line with Zhao (2004). The orbital arc length was set equal to six hours. The  
535 orbit computation included a least-squares estimation of the initial state  
536 vector elements and accelerometer’s bias parameters per arc as well as of  
537 accelerometer’s scaling factors per month. This estimation was done by fit-  
538 ting the orbits to input kinematic orbits or reduced-dynamic orbits. For the

539 time interval February 2003 – December 2005, reduced-dynamic orbits were  
 540 exploited as input, which were kindly provided by Kroes et al. (2005). For  
 541 the rest of the time interval, kinematic orbits were exploited, which were  
 542 produced in the GNSS Research Center of Wuhan University in line with  
 543 Zhao (2004).

544 Observed inter-satellite ranges were obtained from the second release of  
 545 GRACE level-1B data. These data are biased due to phase ambiguities. The  
 546 dynamic orbits were used to estimate a bias per continuous data segment  
 547 by least-squares. In addition, the dynamic orbits were used to compute a  
 548 priori inter-satellite ranges. Subsequently, residual inter-satellite ranges were  
 549 obtained by subtracting the a priori inter-satellite ranges from the observed  
 550 bias-corrected ones. Finally, the residual inter-satellite ranges were used to  
 551 compute residual range combinations in line with Eq. A.1.

The obtained residual range combinations suffer from a low-frequency noise below 2 – 3 cycles per revolution (cpr) (e.g., Liu, 2008), which is mainly caused by dynamic orbit errors (Ditmar et al., 2012). This noise was approximated per orbital revolution with a seven-parameter function used earlier in (e.g., Kim, 2000; Liu et al., 2010):

$$r(t) = x_0 + x_1 t + x_2 \cos \omega t + x_3 \sin \omega t + x_4 t \cos \omega t + x_5 t \sin \omega t + x_6 t^2. \quad (\text{A.2})$$

552 Herein,  $\omega = \frac{2\pi}{T}$  is the orbital angular velocity with  $T$  being the orbital pe-  
 553 riod. The unknowns  $x_0 \dots x_6$  were estimated from residual data using least-  
 554 squares. Thereafter, the estimated model was removed from the residuals.  
 555 Note that time-varying gravity field signals, which are to be retrieved at a

556 later stage, play a role of noise in the context of this least-squares adjustment.  
557 If the presence of this noise is ignored, as it was done when computing DMT-  
558 1, the estimated function will tend to explain not only the low-frequency  
559 noise in the residuals, but also a part of time-varying gravity field signals.  
560 Consequently, these signals may be partly removed from the data. In partic-  
561 ular, this concerns signals associated with spherical harmonic degrees below 4  
562 (Farahani et al., 2013a). To mitigate this effect, the least-squares adjustment  
563 was performed with a spatially-dependent data weighting, whose details are  
564 provided in (Farahani et al., 2014). The scheme ensures that residual data  
565 collected over areas with minor mass variations (e.g., in the oceanic areas  
566 and deserts) get the largest weights in this adjustment.

## 567 **Appendix B. Computing DMT-2 clone to degree 96**

568 To compute clones of DMT-2 monthly gravity field solutions to degree  
569 96, we begin with the original DMT-2 unconstrained solutions, which are  
570 complete to degree 120, and their noise covariance matrices. We first compute  
571 the right-hand side vectors of the systems of linear equations associated with  
572 the monthly unconstrained solutions to degree 120

$$\mathbf{u}_{(k)}^{120} = (\mathbf{C}_{\hat{\mathbf{x}}(k)}^{120})^{-1} \hat{\mathbf{x}}_{(k)}^{120}, \quad (\text{B.1})$$

573 with  $\hat{\mathbf{x}}_{(k)}^{120}$  and  $\mathbf{C}_{\hat{\mathbf{x}}(k)}^{120}$  being respectively the unconstrained solution to degree  
574 120 and its noise covariance matrix for month  $k$ . A truncation of  $\mathbf{u}_{(k)}^{120}$  and  
575  $(\mathbf{C}_{\hat{\mathbf{x}}(k)}^{120})^{-1} = \mathbf{N}_{(k)}^{120}$ , i.e., the corresponding normal matrix, at degree 96, which  
576 can be done with ease, allows monthly unconstrained solutions to degree 96  
577 to be computed

$$\hat{\mathbf{x}}_{(k)}^{96} = \mathbf{C}_{\hat{\mathbf{x}}(k)}^{96} \mathbf{u}_{(k)}^{96}, \quad (\text{B.2})$$

578 with  $\mathbf{C}_{\hat{\mathbf{x}}^{(k)}}^{96} = \left(\mathbf{N}_{(k)}^{96}\right)^{-1}$  being the noise covariance matrix of  $\hat{\mathbf{x}}_{(k)}^{96}$ . Herein,  
579  $\mathbf{N}_{(k)}^{96}$  and  $\mathbf{u}_{(k)}^{96}$  respectively symbolize the monthly normal matrices and right-  
580 hand-side vectors truncated at degree 96.

## 581 **References**

582 Bamber JL, Riva REM, Vermeersen BLA, LeBrocq AM (2009) Reassessment  
583 of the potential sea-level rise from a collapse of the West Antarctic ice sheet,  
584 *Science*, 324: 901–903, doi: 10.1126/science.1169335.

585 Baur O, Sneeuw N (2011) Assessing Greenland ice mass loss by means of  
586 point-mass modeling: a viable methodology, *J Geod*, 85: 607–615, doi:  
587 10.1007/s00190-011-0463-1.

588 Bettadpur S (2007) CSR Level-2 processing standards document for product  
589 release 04, GRACE 327-742, Revision 3.1.

590 Bettadpur S (2012) CSR level-2 processing standards document for level-2  
591 product release 05, GRACE 327-742.

592 Bruinsma SL, Lemoine J-M, Biancale R, Valès N (2010) CNES/GRGS 10-  
593 day gravity field models (release 2) and their evaluation, *Adv Space Res*,  
594 45: 587–601, doi: 10.1016/j.asr.2009.10.012.

595 Case K, Kruizinga GLH, Wu S-C (2004) GRACE Level-1B data product user  
596 handbook, Jet Propulsion Laboratory, California Institute of Technology,  
597 JPL D-22027.



- 598 Chen Q, Shen Y, Zhang X, Hsu H, Chen W, Ju X, Lou L (2015) Monthly grav-  
599 ity field models derived from GRACE level 1B data using a modified short-  
600 arc approach, *J Geophys Res*, 120, 1804–1819, doi: 10.1002/2014JB011470.
- 601 Dahle C, Flechtner F, Gruber C, König D, König R, Michalak G, Neumayer  
602 K-H (2012) GFZ GRACE level-2 processing standards document for level-2  
603 product release 05, Technical Report STR12/02, doi: 10.2312/GFZ.b103-  
604 12020.
- 605 Desai SD (2002) Observing the pole tide with satellite altimetry, *J Geophys*  
606 *Res*, 107(C11), 3186, doi: 10.1029/2001JC001224.
- 607 Ditmar P, van Eck van der Sluijs AA (2004) A technique for modeling the  
608 Earth’s gravity field on the basis of satellite accelerations, *J Geod*, 78:  
609 12–33, doi: 10.1007/s00190-003-0362-1.
- 610 Ditmar P, Kuznetsov V, van Eck van der Sluijs AA, Schrama E, Klees R  
611 (2006) DEOS\_CHAMP-01C-70: a model of the Earth’s gravity field com-  
612 puted from accelerations of the CHAMP satellite, *J Geod*, 79: 586–601,  
613 doi: 10.1007/s00190-005-0008-6.
- 614 Ditmar P, Teixeira da Encarnação J, Farahani HH (2012) Understanding data  
615 noise in gravity field recovery on the basis of inter-satellite ranging mea-  
616 surements acquired by the satellite gravimetry mission GRACE, *J Geod*,  
617 86: 441–465, doi: 10.1007/s00190-011-0531-6.
- 618 Dobsław H, Flechtner F, Bergmann-Wolf I, Dahle C, Dill R, Esselborn S,  
619 Sasgen I, Thomas M (2013) Simulating high-frequency atmosphere-ocean

- 620 mass variability for de-aliasing of satellite gravity observations: AOD1B  
621 RL05, *J Geophys Res*, 118: 3704–3711, doi: 10.1002/jgrc.20271.
- 622 Farahani HH (2013) Modelling the Earth’s static and time-varying grav-  
623 ity field using a combination of GRACE and GOCE data, PhD  
624 Thesis, Delft University of Technology, Delft, The Netherlands, doi:  
625 10.13140/RG.2.1.3104.3286.
- 626 Farahani HH, Ditmar P, Klees R, Liu X, Zhao Q, Guo J (2013a) The static  
627 gravity field model DGM-1S from GRACE and GOCE data: computation,  
628 validation and an analysis of GOCE mission’s added value, *J Geod*, 87:  
629 843–867, doi: 10.1007/s00190-013-0650-3.
- 630 Farahani HH, Ditmar P, Klees R, Teixeira da Encarnação J, Liu X, Zhao Q,  
631 Guo J (2013b) Validation of static gravity field models using GRACE K-  
632 band ranging and GOCE gradiometry data, *Geophys J Int*, 194: 751–771,  
633 doi: 10.1093/gji/ggt149.
- 634 Farahani HH, Ditmar P, Klees R (2014) Assessment of the added value of data  
635 from the GOCE satellite mission to time-varying gravity field modeling, *J*  
636 *Geod*, 88: 157–178, doi: 10.1007/s00190-013-0674-8.
- 637 Felikson D, Urban TJ, Pie N, Gunter B, Harpold R, Schutz BE (2016)  
638 Comparison of repeat track, crossover, and overlapping footprint eleva-  
639 tion change methods from satellite altimetry: ICESat-1 elevation changes  
640 of Greenland and Antarctica (in review).
- 641 Flechtner F (2007) GFZ Level-2 processing standards document for product  
642 release 04, GRACE 327-743, GR-GFZ-STD-001.

- 643 Gunter BC, Wittwer T, Stolk W, Klees R, Ditmar P (2009) Comparison of re-  
644 gional and global GRACE gravity field models at high latitudes, in Kenyon  
645 S, Pacino MC, Marti U (eds.), *Geodesy for Planet Earth*, International  
646 Association of Geodesy Symposia 136, pp. 171–177, doi: 10.1007/978-3-  
647 642-20338-1\_21.
- 648 Gunter BC, Didova O, Riva REM, Ligtenberg SRM, Lenaerts JTM, King  
649 MA, van den Broeke MR, Urban T (2014) Empirical estimation of present-  
650 day Antarctic glacial isostatic adjustment and ice mass change, *The*  
651 *Cryosphere*, 8: 743–760, doi: 10.5194/tc-8-743-2014.
- 652 Han S-C, Shum CK, Bevis M, Ji C, Kuo1 C-Y (2006) Crustal dilatation ob-  
653 served by GRACE after the 2004 Sumatra-Andaman earthquake, *Science*,  
654 313: 658–662, doi: 10.1126/science.1128661.
- 655 Han S-C, Sauber J, Riva REM (2011) Contribution of satellite gravimetry  
656 to understanding seismic source processes of the 2011 Tohoku-Oki earth-  
657 quake, *Geophys Res Lett*, 38, L24312, doi: 10.1029/2011GL049975.
- 658 Jekeli C (1981) Alternative methods to smooth the Earth’s gravity field,  
659 Technical Report No. 327, Ohio State University, Columbus, Ohio, USA.
- 660 Joughin I, Tulaczyk S (2002) Positive mass balance of the Ross ice streams,  
661 West Antarctica, *Science* 295: 476–480, doi: 10.1126/science.1066875.
- 662 Kim J (2000) Simulation study of a low-low satellite-to-satellite tracking  
663 mission, PhD Thesis, Center for Space Research, The University of Texas  
664 at Austin, Texas, USA.

- 665 Klees R, Broersen P (2002) How to handle colored noise in large least-squares  
666 problems – Building the optimal filter, Delft University Press, DUP Sci-  
667 ence, Delft, The Netherlands.
- 668 Klees R, Ditmar P, Broersen P (2003) How to handle colored observa-  
669 tion noise in large least-squares problems, *J Geod*, 76: 629–640, doi:  
670 10.1007/s00190-002-0291-4.
- 671 Klees R, Ditmar P (2004) How to handle colored noise in large least-squares  
672 problems in the presence of data gaps? in Sansò F (ed.), *V Hotine-*  
673 *Marussi Symposium on Mathematical Geodesy*, International Association  
674 of Geodesy Symposia, vol. 127, pp. 39–48, doi: 10.1007/978-3-662-10735-  
675 5\_6.
- 676 Klees R, Zapreeva EA, Winsemius HC, Savenije HHG (2007) The bias in  
677 GRACE estimates of continental water storage variations, *Hydrol Earth*  
678 *Syst Sci*, 11: 1227–1241, doi: 10.5194/hess-11-1227-2007.
- 679 Klees R, Liu X, Wittwer T, Gunter BC, Revtova EA, Tenzer R, Ditmar  
680 P, Winsemius HC, Savenije HHG (2008a) A comparison of global and  
681 regional GRACE models for land hydrology, *Surv Geophys*, 29: 335–359,  
682 doi: 10.1007/s10712-008-9049-8.
- 683 Klees R, Revtova EA, Gunter BC, Ditmar P, Oudman E, Winsemius  
684 HC, Savenije HHG (2008b) The design of an optimal filter for monthly  
685 GRACE gravity models, *Geophys J Int*, 175: 417–432, doi: 10.1111/j.1365-  
686 246X.2008.03922.x.

- 687 Kroes R, Montenbruck O, Bertiger W, Visser P (2005) Precise GRACE base-  
688 line determination using GPS, *GPS Solut*, 9: 21–31, doi: 10.1007/s10291-  
689 004-0123-5.
- 690 Kurtenbach E, Mayer-Gürr T, Eicker A (2009) Deriving daily snapshots of  
691 the Earth’s gravity field from GRACE L1B data using Kalman filtering,  
692 *Geophys Res Lett*, 36, L17102, doi: 10.1029/2009GL039564.
- 693 Kusche J (2007) Approximate decorrelation and non-isotropic smoothing of  
694 time-variable GRACE-type gravity field models, *J Geod*, 81: 733–749, doi:  
695 10.1007/s00190-007-0143-3.
- 696 Kusche J, Schmidt R, Petrovic S, Rietbroek R (2009) Decorrelated GRACE  
697 time-variable gravity solutions by GFZ, and their validation using a hy-  
698 drological model, *J Geod*, 83: 903–913, doi: 10.1007/s00190-009-0308-3.
- 699 Lenaerts JTM, van den Broeke MR, van de Berg WJ, van Meijgaard E,  
700 Munneke PK (2012) A new, high-resolution surface mass balance map of  
701 Antarctica (19792010) based on regional atmospheric climate modeling,  
702 *Geophys Res Lett*, 39, L04501, doi: 10.1029/2011GL050713.
- 703 Ligtenberg, SRM, Helsen MM, van den Broeke MR (2011) An improved semi-  
704 empirical model for the densification of Antarctic firn, *The Cryosphere*, 5:  
705 809–819, doi: 10.5194/tc-5-809-2011.
- 706 Liu X (2008) Global gravity field recovery from satellite-to-satellite track-  
707 ing data with the acceleration approach, PhD Thesis, Delft University of  
708 Technology, Delft, The Netherlands.

- 709 Liu X, Ditmar P, Siemes C, Slobbe DC, Revtova E, Klees R, Riva R, Zhao  
710 Q (2010) DEOS Mass Transport model (DMT-1) based on GRACE satel-  
711 lite data: methodology and validation, *Geophys J Int*, 181: 769–788, doi:  
712 10.1111/j.1365-246X.2010.04533.x.
- 713 Luthcke SB, Zwally HJ, Abdalati W, Rowlands DD, Ray RD, Nerem RS,  
714 Lemoine FG, McCarthy JJ, Chinn DS (2006) Recent Greenland ice mass  
715 loss by drainage system from satellite gravity observations, *Science*, 314:  
716 1286–1289, doi: 10.1126/science.1130776.
- 717 Luthcke SB, Sabaka TJ, Loomis BD, Arendt AA, McCarthy JJ, Camp J  
718 (2013) Antarctica, Greenland and Gulf of Alaska land ice evolution from  
719 an iterated GRACE global mascon solution, *J Glaciol*, 59: 613–631, doi:  
720 10.3189/2013JoG12J147.
- 721 Mayer-Gürr T (2006) Gravitationsfeldbestimmung aus der Analyse kurzer  
722 Bahnbögen am Beispiel der Satellitenmissionen CHAMP und GRACE,  
723 PhD Thesis, University of Bonn, Bonn, Germany.
- 724 Mayer-Gürr T, Eicker A, Kurtenbach E, Ilk K-H (2010a) ITG-GRACE:  
725 Global static and temporal gravity field models from GRACE data, in  
726 Flechtner F, Gruber T, Güntner A, Manda M, Rothacher M, Schöne  
727 T, Wickert J (eds.), *System Earth via Geodetic-Geophysical Space Tech-  
728 niques*, pp. 159–168, doi: 10.1007/978-3-642-10228-8\_13.
- 729 Mayer-Gürr T, Eicker A, Kurtenbach E (2010b) ITG-Grace2010: The new  
730 GRACE gravity field release computed in Bonn, *Geophys Res Abs*, 12,  
731 EGU2010-2446.

- 732 Mayer-Gürr T, Zehentner N, Klinger B, Kvas A (2014) ITSG-Grace2014: a  
733 new GRACE gravity field release computed in Graz, in GRACE Science  
734 Team Meeting, Potsdam, Germany.
- 735 Meyer U, Jäggi A, Beutler G (2012) Monthly gravity field solutions based on  
736 GRACE observations generated with the Celestial Mechanics Approach,  
737 Earth Planet Sc Lett, 345: 72–80, doi: 10.1016/j.epsl.2012.06.026.
- 738 McCarthy DD, Petit G (2004) IERS conventions (2003) IERS Technical Note  
739 32, Verlag des Bundesamtes für Kartographie und Geodäsie, Frankfurt am  
740 Main, Germany.
- 741 Heiskanen WA, Moritz H (1967) Physical Geodesy, Bull Geodesique, 86: 491,  
742 doi: 10.1007/BF02525647.
- 743 Rignot E, Mouginot J (2012) Ice flow in Greenland for the Interna-  
744 tional Polar Year 2008–2009, Geophys Res Lett, 39, L11501, doi:  
745 10.1029/2012GL051634.
- 746 Savcenko R, Bosch W (2012) EOT11a – Empirical ocean tide model from  
747 multi-mission satellite altimetry, Report No. 89, Deutsches Geodätisches  
748 Forschungsinstitut (DGFI), München, Germany.
- 749 Siemes C, Ditmar P, Riva REM, Slobbe DC, Liu X, Farahani HH (2013)  
750 Estimation of mass change trends in the Earth’s system on the basis of  
751 GRACE satellite data, with application to Greenland, J Geod, 87: 69–87,  
752 doi: 10.1007/s00190-012-0580-5.
- 753 Standish EM (1998) JPL planetary and lunar ephemerides, DE405/LE405,  
754 Jet Propulsion Labratory, IOM 312.F – 98 – 048.

- 755 Sun Y, Riva R, Ditmar P (2016) Optimizing estimates of annual variations  
756 and trends in geocenter motion and J2 from a combination of GRACE  
757 data and geophysical models, *J Geophys Res* (in review).
- 758 Swenson S, Wahr J, Milly PCD (2003) Estimated accuracies of regional  
759 water storage variations inferred from the Gravity Recovery and Cli-  
760 mate Experiment (GRACE), *Water Resour Res*, 39(8), 1223, doi:  
761 10.1029/2002WR001808.
- 762 Swenson S, Chambers D, Wahr J (2008) Estimating geocenter variations from  
763 a combination of GRACE and ocean model output, *J Geophys Res*, 113,  
764 B08410, doi: 10.1029/2007JB005338.
- 765 Tapley BD, Bettadpur S, Watkins M, Reigber C (2004a) The gravity recovery  
766 and climate experiment: Mission overview and early results, *Geophys Res*  
767 *Lett*, 31, L09607, doi: 10.1029/2004GL019920.
- 768 Tapley BD, Bettadpur S, Ries JC, Thompson PF, Watkins MM (2004b)  
769 GRACE measurements of mass variability in the Earth system, *Science*,  
770 305: 503–505, doi: 10.1126/science.1099192.
- 771 Wahr J, Molenaar M, Bryan F (1998) Time variability of the Earth’s  
772 gravity field: Hydrological and oceanic effects and their possible de-  
773 tection using GRACE, *J Geophys Res*, 103(B12): 30205–30229, doi:  
774 10.1029/98JB02844.
- 775 van der Wal W, Wu P, Sideris MG, Shum CK (2008) Use of GRACE de-  
776 termined secular gravity rates for glacial isostatic adjustment studies in  
777 North-America, *J Geodyn*, 46: 144–154, doi: 10.1016/j.jog.2008.03.007.



- 778 Watkins MM, Yuan D (2007) JPL level-2 processing standards document for  
779 product release 04, GRACE 327-744.
- 780 Watkins MM, Yuan D (2012) JPL level-2 processing standards document for  
781 product release 05, GRACE 327-744.
- 782 Watkins MM, Wiese DN, Yuan D-N, Boening C, Landerer FW (2015) Im-  
783 proved methods for observing Earth's time variable mass distribution with  
784 GRACE using spherical cap mascons, *J Geophys Res*, 120, 2648–2671, doi:  
785 10.1002/2014JB011547.
- 786 Whitehouse PL, Bentley MJ, Milne GA, King MA, Thomas ID (2012) A new  
787 glacial isostatic adjustment model for Antarctica: calibrated and tested  
788 using observations of relative sea-level change and present-day uplift rates,  
789 *Geophys J Int* 190: 1464–1482, doi: 10.1111/j.1365-246X.2012.05557.x.
- 790 Wouters B, Chambers D, Schrama EJO (2008) GRACE observes small-  
791 scale mass loss in Greenland, *Geophys Res Lett*, 35, L20501, doi:  
792 10.1029/2008GL034816.
- 793 Zhao Q (2004) Research on precise orbit determination theory and software  
794 for both GPS navigation constellation and LEO satellites, PhD Thesis,  
795 Wuhan University, Wuhan, China.